

Orbit Determination Accuracy for Comets  
on Earth-Impacting Trajectories

by

Linda Kay-Bunnell

B.S. Aerospace Engineering, May 2000

Florida Institute of Technology

A Thesis Submitted to

The Faculty of the School of Engineering and Applied Science

of

The George Washington University

in partial fulfillment of the requirements for the degree of

Master of Science

May 18, 2003

Thesis directed by

Robert H. Tolson

Professor of Engineering and Applied Science

This research was conducted at NASA Langley Research Center, Hampton, Virginia

## Abstract

Recently, there has been increased interest in the possibility of asteroids and comets impacting the Earth. These studies have ranged from orbit determination to mitigation, mostly concentrating on near Earth asteroids, or NEAs. NEA orbits can usually be determined very accurately because many observations are available over several orbital periods. It is possible that an asteroid or comet will be discovered on the inbound leg of an impacting trajectory, with only a limited amount of time available to collect observations to determine the orbit, and is a likely scenario for a long-period comet. Also, unlike NEAs, comet trajectories are perturbed by outgassing forces, which are exerted when the comet surface materials are sublimated by the radiation of the Sun. The results presented in this paper show the level of orbit determination accuracy obtainable for long-period comets discovered approximately one year before collision, including non-gravitational perturbations due to outgassing. Comet orbits are designed to impact the center of the Earth, and preliminary orbits are determined from simulated observations using Gauss' method. Additional measurements are incorporated to improve the orbit solution through the use of a Kalman filter. A comparison is made between observatories in several different circular heliocentric orbits, and shows that observatories in orbits with radii less than 1 AU result in increased orbit determination accuracy for short tracking durations due to increased parallax per unit time. However, an observatory in a circular heliocentric orbit at 1 AU will perform just as well if the tracking duration is increased, and the orbit determination accuracy is significantly improved if additional observatories are positioned at the Sun-Earth Lagrange points  $L_3$ ,  $L_4$ , or  $L_5$ . A single observatory at 1 AU capable of both optical and range measurements yields the highest orbit determination accuracy in the shortest amount of time when compared to other systems of observatories in circular heliocentric orbits at 1 AU.

## Acknowledgements

The author wishes to extend thanks to all those whose time, patience, and insight contributed to this challenging and rewarding project. To professor Robert Tolson, whose natural intellect and many years of experience proved to be invaluable resources throughout every aspect of this research. His guidance and direction were essential elements in bringing this work into a focused study, and his encouraging and witty remarks provided an extra boost in motivation at just the right times. To Carlos Roithmayr, for taking the time to explain difficult concepts in a way that would instantly enlighten my understanding. Much of the subject material presented here is a direct result of our discussions. The example of his careful and thorough approach to this study is a standard I will strive to uphold in years to come. To Dan Mazanek and all the members of the Spacecraft & Sensors Branch at NASA Langley Research Center, and also to Renjith Kumar and Hans Seywald of Analytical Mechanics Associates, Inc., for their patience and for the manner in which they planned project schedules so that completion of this research could be a priority. To my family and friends, for their encouragement and genuine interest in my education and in my career. Especially to my parents, whose unwavering support has been, and will continue to be, an infinite source of strength to draw upon and an inspiration for setting high goals and persevering to meet them. And finally, to my husband Adam Bunnell, for his willingness to alter his own career for the sake of the advancement of mine, for the countless personal compromises he made voluntarily over the years in support of this endeavor, and for the unconditional love and understanding he expressed on a daily basis. I can only hope that a lifetime spent trying is enough time to reciprocate his selfless devotion.

# Table of Contents

Abstract .....	ii
Acknowledgements .....	iii
Table of Contents .....	iv
List of Figures .....	vi
List of Tables.....	viii
Nomenclature .....	ix
1 Introduction .....	1
2 Orbital Motion.....	4
2.1 The N-Body Problem .....	4
2.2 The Two-body Problem .....	7
2.3 Orbit Propagation .....	9
2.4 Perturbing Forces .....	11
3 Impact Trajectory Criteria.....	17
3.1 Warning Time .....	17
3.2 Designing Earth-Impacting Orbits .....	20
4 Orbit Determination and Collision Probability .....	22
4.1 Methods of Orbit Determination.....	23
4.1.1 Preliminary Orbit Determination Using Gauss' Method .....	24
4.1.2 Final Orbit Determination Using the Kalman Filter .....	26
4.1.2.1 State Propagation.....	27

4.1.2.2	The Observation Equation.....	29
4.1.2.3	Time and Measurement Updates.....	31
4.2	Orbit Determination Accuracy .....	34
4.2.1	The B-plane .....	35
4.2.2	State Uncertainties at Nominal Collision Time.....	38
4.2.3	Position Uncertainty in the B-plane .....	39
4.2.4	Validation of Linearity .....	40
4.2.5	Collision Probability .....	44
5	Observatory Location and Observation Schedule.....	49
5.1	Single Observatory at Earth .....	50
5.2	Single Observatory in a Circular Orbit at 1 AU.....	54
5.3	Multiple Observatories in Circular Orbits at 1 AU.....	60
6	Summary and Conclusions.....	66
7	Future Work .....	68
	References .....	69
	Appendix .....	70

## List of Figures

Figure 1. Inertial reference frame unit vectors .....	7
Figure 2. Deviation in position due to outgassing forces for a long-period comet .....	15
Figure 3. Deviation in position due to outgassing forces for a short-period comet .....	16
Figure 4. Orbits of the Earth and an impacting comet .....	18
Figure 5. Times of flight between detection and collision for short- and long-period comets.....	20
Figure 6. B-plane geometry.....	35
Figure 7. Error ellipse for a sample long-period comet after 91 observations ( $1\sigma$ ).....	41
Figure 8. Error ellipse for a sample short-period comet after 91 observations ( $1\sigma$ ).....	42
Figure 9. Variation in error ellipse parameters for a sample long-period comet after 91 observations.....	43
Figure 10. Variation in error ellipse parameters for a sample short-period comet after 91 observations.....	43
Figure 11. Earth collision probability for a sample long-period comet after 91 observations.....	46
Figure 12. Maximum collision probability as a function of tracking duration for sample long- and short-period comets.....	47
Figure 13. Maximum collision probability as a function of tracking duration on a logarithmic scale for sample long- and short-period comets .....	48
Figure 14. Earth collision probability for a sample long-period comet after 141 observations.....	48
Figure 15. Collision probability results from a single Earth observatory .....	50
Figure 16. Collision probability for central and limb impacts .....	51

Figure 17. Collision probability results from a single Earth observatory on a logarithmic scale.....	52
Figure 18. Orbit geometry between an observatory at 1 AU and direct and retrograde comets.....	53
Figure 19. Orientation of error ellipses for a long-period comet with 45° inclination ....	54
Figure 20. Semimajor axis of error ellipse after 5 observations as a function of the angle between the observatory and the Sun-comet line.....	55
Figure 21. Semimajor axis of error ellipse after 5 observations as a function of time rate of change of parallax .....	56
Figure 22. Time rate of change of parallax as a function of observatory orbit radius for a hypothetical comet with $i = 0^\circ$ .....	57
Figure 23. Collision probability as a function of tracking duration for Mercury, Venus, Earth, and Mars observatories .....	58
Figure 24. Collision probability as a function of tracking duration for Mercury, Venus, Earth, and Mars observatories on a logarithmic scale.....	59
Figure 25. Location of Sun-Earth Lagrange points.....	60
Figure 26. Collision probability results from observatories in circular heliocentric orbits at 1 AU .....	61
Figure 27. Orbit geometry for range measurements .....	63
Figure 28. Error in heliocentric distance of comet.....	64
Figure A1. Orbital plane orientation in 3-dimensional space .....	70

## List of Tables

Table 1. Error Ellipse Parameters for Sample Long- and Short-Period Comets.....	44
Table 2. Error Ellipse Parameters for Sample Long- and Short-Period Comets with Outgassing Included.....	44

## Nomenclature

$a$	Semimajor axis
$A_i$	Outgassing coefficients
AU	Astronomical Unit
<b>B</b>	Miss vector in the B-plane
B	Miss distance in the B-plane
$c$	Outgassing normalizing constant
<b>d</b>	Position of observatory
<b>e</b>	Eccentricity vector
$e$	Eccentricity
$E$	Eccentric anomaly
$\mathcal{E}$	Energy
<b>f</b>	Force
$f$	Lagrange coefficient
$f_{TR}$	Bivariate Gaussian probability density
$g$	Lagrange coefficient
$G$	Universal gravitational constant
<b>h</b>	Angular momentum vector
$h$	Magnitude of angular momentum
$\tilde{\mathbf{H}}$	Observation matrix
$i$	Inclination
<b>I</b>	Identity matrix

<b>K</b>	Kalman gain matrix
$L_3, L_4, L_5$	Sun-Earth Lagrange points
$m$	Mass
$M$	Mean anomaly
<b>n</b>	Node vector
$n$	Mean motion
NEA	Near Earth Asteroid
$p$	Semi-latus rectum
<b>P</b>	Covariance matrix of error in state deviation estimate
<b>Q</b>	Covariance matrix of error in state model
<b>r</b>	Position vector
$r$	Magnitude of position vector
$r_a$	Radius of apoapsis
$r_c$	Heliocentric collision radius (1 AU)
$r_p$	Radius of periapsis
<b>R</b>	Covariance matrix of error in measurement
$R_E$	Earth radius
$\bar{R}_E$	Effective collision radius of Earth
$t$	Time
$\hat{\mathbf{T}}, \hat{\mathbf{R}}, \hat{\mathbf{S}}$	B-plane unit vectors
$U_i$	Universal variables
<b>v</b>	Velocity vector
$v$	Magnitude of velocity vector

$v_r$	Magnitude of velocity along radial direction
$\mathbf{V}$	Matrix of normalized eigenvectors
$\mathbf{w}$	State deviation error
$\mathbf{x}$	State deviation vector
$\mathbf{y}$	Observation residual vector
$z$	Reciprocal of semimajor axis
$\Phi$	State transition matrix
$\Omega$	Longitude of ascending node
$\alpha$	Acceleration due to comet outgassing
$\beta$	Heliocentric parallax
$\chi$	Generalized anomaly
$\epsilon$	Measurement error
$\gamma$	Angle between observatory and Sun-comet line
$\eta$	Measurement resolution
$\varphi$	Celestial longitude
$\lambda$	Celestial latitude
$\kappa_0$	Collision probability at center of Earth
$\kappa_T$	Collision probability at surface of Earth along $\hat{\mathbf{T}}$
$\kappa_R$	Collision probability at surface of Earth along $\hat{\mathbf{R}}$
$\mu$	Gravitational parameter
$\nu$	True anomaly
$\theta$	Error ellipse orientation

$\rho$	Range
$\rho_{TR}$	Correlation coefficient of $\sigma_T$ and $\sigma_R$
$\sigma_{Ai}$	Standard deviation of random outgassing coefficients
$\sigma_R$	Standard deviation of $B_R$
$\sigma_T$	Standard deviation of $B_T$
$\sigma_1$	Semimajor axis of error ellipse
$\sigma_2$	Semiminor axis of error ellipse
$\sigma_3$	Error in time of arrival to the B-plane
$\tau$	Time of periapsis passage
$\omega$	Argument of periapsis

# 1 Introduction

The “impact” theory is one explanation of the mass extinctions that have occurred throughout the history of the Earth. Many scientists agree that the massive impact crater discovered in the Yucatan peninsula is the result of an extraterrestrial collision responsible for the extinction of the dinosaurs some 65 million years ago. On a clear night the Moon reveals evidence of the devastation caused by asteroid and comet bombardment spanning billions of years, which no doubt still occurs today even if it is on a much more infrequent scale. Much media attention has been given in recent years to the possibility of an Earth impact, and the attention is not unwarranted. The surface of the Earth is still speckled with the scars of past encounters. One of the most visible, although certainly not the largest, is the Barringer Meteor Crater in the Arizona desert. An object 25 – 60 meters in diameter carved out this one kilometer wide crater upon impact 50,000 years ago. In 1908, an object believed to be an asteroid exploded over Tunguska, Siberia, destroying an area of forest larger than the city of Los Angeles. It is estimated that an impact of this magnitude occurs every one hundred years, and that a globally catastrophic impact happens every one million years [1]. Existing craters are evidence that our planet has been hit in the past. It most definitely will be hit in the future. Nothing could have proved this point more than the impact event of comet Shoemaker-Levy 9 with Jupiter in 1994, which left several blemishes on the surface of the planet 2 to 3 times the size of the Earth. This event brought to our attention a threat that perhaps had not been seriously considered – comets.

Most current research is in the area of improving orbit determination for known near-Earth asteroids (NEAs) with Earth-crossing or Earth-approaching orbits, to predict possible collisions many decades into the future. NASA has recently adopted the goal of finding 90%

of the asteroids 1 km and larger by the year 2008 [2]. This goal may very well be realized, since it is possible to observe the asteroids over many orbital periods due to their close proximity to Earth. With the possibility of hundreds of observations over more than one orbital period, the orbits can be calculated with sufficient accuracy to predict collision potential decades into the future [2]. However, there is no current effort to discover long-period comets that may be traveling on Earth-impacting trajectories. A long-period comet is defined as a comet with an orbital period greater than 200 years, and could be thousands or even millions of years. The orbit determination problem for the long-period comet case is much different than that of asteroids, since it is likely that an impacting comet will only be observable for less than half of its orbital period before the collision occurs. Astronomers discovered comet Shoemaker-Levy 9 only 16 months before it collided with Jupiter. It was just enough time to turn the world's telescopes in the direction of our largest neighbor and watch, as the remnants of the comet that the massive gravity of Jupiter tore apart hit the planet in a barrage of explosions. The impacts left behind distortions in the Jovian atmosphere that were visible from Earth for up to a month. Orbit determination for comet Shoemaker-Levy 9 resulted in predictions within 11 minutes or less of actual impact times for all fragments [3].

Orbit determination is the process of collecting a set of measurements and calculating the position and velocity of an object at a particular time, or determining a set of six orbital elements that define the size, shape, and orientation of the orbit of the object. Preliminary orbit determination is performed by using the minimum number of observations required to calculate the orbital parameters, and assuming two-body orbital motion about the Sun. The orbit is then refined by using methods that can incorporate additional measurements and includes a more complete force model including non-gravitational perturbations. The

purpose of the current study is to investigate the accuracy of orbit determination for comets discovered approximately one year before a collision with Earth occurs. Orbits are constructed so that a collision will take place on the inbound leg of the orbit. Preliminary orbits are determined from the minimum number of optical observations of celestial latitude and longitude required to calculate position and velocity at some epoch. More precise orbits are then determined by adding additional optical measurements and observatories, by including radar or laser measurements of range, and by incorporating non-gravitational forces due to comet outgassing into the dynamics model. The effect of the geometry between the observatory and the comet is also investigated by placing the observatory in various locations in circular heliocentric orbits with radii equal to 0.39, 0.72, 1.0, and 1.5 astronomical units (AU), corresponding to Mercury, Venus, Earth, and Mars orbits respectively.

This investigation requires a thorough understanding of gravitational attraction and orbital mechanics, so this topic is discussed in the next section. Orbit geometries are explained and orbital elements are defined in the Appendix. Sec. 3 focuses on warning time and collision design criteria. Orbit determination and accuracy are discussed in Sec. 4. Orbit determination results obtained by optical measurements of angular position are examined for a family of representative comet orbits in Sec. 5, along with results obtained by including additional radar information and perturbative effects. Conclusions and suggestions for further study are presented in Secs. 6 and 7.

## 2 Orbital Motion

The  $N$ -body problem in orbital mechanics is the problem of solving the equations of motion for  $N$  bodies in space, and is formulated using Newton's laws. The two-body problem is a simplification of the  $N$ -body problem, for which a complete analytic solution can be found. There are numerous approaches to the development of and the solution for the two-body equations of motion. The method discussed in the next two sections follows the general approach described in detail in Refs. [4] and [5]. It will be seen that the two-body simplification requires external forces such as comet outgassing to be neglected, so a method for including these perturbative forces in comet orbit determination is described in Sec. 2.4.

### 2.1 The $N$ -Body Problem

Newton's laws of motion are [5]:

*First Law*      *Every body continues in its state of rest, or of uniform motion in a straight line, unless it is compelled to change that state by a force impressed upon it.*

*Second Law*    *The rate of change of momentum is proportional to the force impressed, and is in the same direction as that force.*

*Third Law*      *To every action there is always opposed an equal reaction.*

These three laws of motion were first introduced in 1687 with the publication of *Principia*, although Newton had worked out the equations some 20 years earlier. Also introduced was his law of universal gravitation, which states that any two bodies attract one another with a force proportional to the product of their masses and inversely proportional to the square of the distance between them. Newton formed these laws with the assumption that the bodies

were particles, or point masses. Also, the laws are only valid in an inertial reference frame, or a reference frame that is at rest or moving with constant velocity. In reality, an inertial reference frame does not exist. For practical applications, a reference frame is considered to be inertial as long as the observed motion of the particles under study agrees with Newton's theoretical prediction of the motion described by his laws.

The motion of a system of  $N$  bodies can be described analytically using Newton's second law of motion and the law of universal gravitation under the assumptions stated above. The gravitational force acting on a body with mass  $m_i$  due to other bodies in the system with masses  $m_1, m_2, \dots, m_N$  is expressed mathematically using Newton's law of universal gravitation as

$$\mathbf{f}_i = G \sum_{\substack{j=1 \\ j \neq i}}^N \frac{m_i m_j}{r_{ij}^3} (\mathbf{r}_j - \mathbf{r}_i), \quad i = 1, \dots, N, \quad (2.1)$$

where  $G$  is the universal gravitational constant and has a value of  $6.672 \times 10^{-11} \text{ Nm}^2/\text{kg}^2$ ,  $\mathbf{r}_i$  is the position vector from the origin of the inertial coordinate frame to the body on which the force is being exerted,  $\mathbf{r}_j$  is the position vector from the origin of the inertial coordinate frame to the body exerting the gravitational force, and  $r_{ij}$  is the distance between the  $i$ -th and  $j$ -th bodies, where

$$\mathbf{r}_{ij} = \mathbf{r}_j - \mathbf{r}_i. \quad (2.2)$$

Newton's second law of motion states that the total force acting on the body is

$$\mathbf{f}_i = m_i \frac{d^2 \mathbf{r}_i}{dt^2} \equiv m_i \frac{d\mathbf{v}_i}{dt} \quad (2.3)$$

where  $\frac{d^2 \mathbf{r}_i}{dt^2}$  and  $\mathbf{v}_i$  are the inertial acceleration and velocity of the body, respectively.

Assuming no other external forces are acting on the system, the expression describing the motion of a system of  $N$  particles is given by

$$\frac{d^2 \mathbf{r}_i}{dt^2} = G \sum_{\substack{j=1 \\ j \neq i}}^N \frac{m_j}{r_{ij}^3} (\mathbf{r}_j - \mathbf{r}_i). \quad (2.4)$$

There is no known general solution to Eq. (2.4). A complete solution requires  $6N$  integrals, of which only 10 are obtainable. The 10 constants of integration result from the fact that total linear momentum, angular momentum, and energy of the system are conserved. From the conservation of total linear momentum it can be shown that the center of mass (CM) of the system moves with constant linear velocity, and that the position of the CM as a function of time is

$$\mathbf{r}(t) = \mathbf{v}_0(t - t_0) + \mathbf{r}_0, \quad (2.5)$$

where  $\mathbf{v}_0$  and  $\mathbf{r}_0$  represent 6 of the constants of integration. The total angular momentum,  $\mathbf{h}$ , of the system is

$$\mathbf{h} = \sum_{i=1}^N \mathbf{r}_i \times m_i \mathbf{v}_i, \quad (2.6)$$

which can be shown to be conserved so that  $\mathbf{h}$  represents three more of the constants of integration. The tenth constant is the total system energy,  $\mathcal{E}$ , which is the sum of the total kinetic and potential energy of the system. Complete derivations and proofs of the

conservation of total linear momentum, angular momentum, and system energy are presented in detail in Ref. [4].

An analytical solution can be found for Eq. (2.4) for the relative motion of two particles under their mutual gravitational attraction. All other forces acting on the particles, including  $N$ -body gravitational attraction, can be described in terms of perturbations. For this reason, the simplified approach of solving the equations of motion for two bodies is ideal for describing the motion of comets in orbit about the Sun.

## 2.2 The Two-body Problem

The inertial reference frame containing the two bodies (the Sun and the comet) is defined by three orthogonal unit vectors,  $\hat{i}_x$ ,  $\hat{i}_y$ , and  $\hat{i}_z$ . Positive  $\hat{i}_z$  is normal to the ecliptic plane and points in a direction parallel to the orbital angular momentum vector of the Earth, positive  $\hat{i}_x$  points in the direction of Earth vernal equinox and lies in the ecliptic plane, and positive  $\hat{i}_y$  lies in the ecliptic plane and completes the orthogonal coordinate system. The mass of the

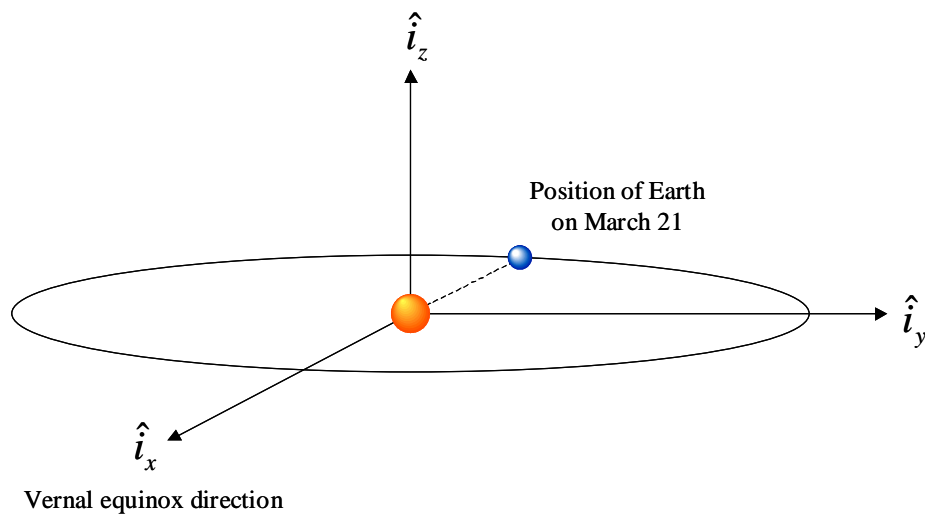


Figure 1. Inertial reference frame unit vectors

comet is negligible compared to the mass of the Sun. The only perturbative effects to be included in determining the comet orbits are those due to outgassing because they are unknown; gravitational attraction from the planets in the solar system, including Earth, can be modeled very precisely and therefore are not considered.

The equations of motion for two bodies are given by Eq. (2.4) with  $N = 2$  and  $i = 1, 2$ , i.e.,

$$m_1 \frac{d^2 \mathbf{r}_1}{dt^2} = G \frac{m_1 m_2}{r_{12}^3} (\mathbf{r}_2 - \mathbf{r}_1) \quad (2.7)$$

and

$$m_2 \frac{d^2 \mathbf{r}_2}{dt^2} = G \frac{m_2 m_1}{r_{21}^3} (\mathbf{r}_1 - \mathbf{r}_2). \quad (2.8)$$

The equation of relative motion for the two-body problem is found by subtracting Eq. (2.8) from Eq. (2.7) to obtain

$$\frac{d^2 \mathbf{r}}{dt^2} = -G \frac{(m_1 + m_2)}{r^3} \mathbf{r}, \quad (2.9)$$

where  $\mathbf{r} = \mathbf{r}_2 - \mathbf{r}_1$ , and  $r$  is the magnitude of  $\mathbf{r}$ . The term  $G(m_1 + m_2)$  is called the gravitational parameter and is represented by  $\mu$ . With this substitution, Eq. (2.9) becomes

$$\frac{d^2 \mathbf{r}}{dt^2} + \frac{\mu}{r^3} \mathbf{r} = \mathbf{0}. \quad (2.10)$$

Eq. (2.10) is a second order, nonlinear, vector differential equation describing the relative motion of two bodies. Even though it is nonlinear, it is possible to find a completely analytic solution to this equation through six independent constants of integration. These six

constants can be the components of position and velocity, or they can be a set of six parameters that define the orbit of the object around the primary body, called orbital elements. Orbital elements are described in detail in the Appendix.

## 2.3 Orbit Propagation

If the position and velocity of an object are known at some time  $t_0$ , the position and velocity can be calculated at any time  $t$  using the expressions

$$\mathbf{r} = f\mathbf{r}_0 + g\mathbf{v}_0, \quad (2.11)$$

$$\mathbf{v} = \dot{f}\mathbf{r}_0 + \dot{g}\mathbf{v}_0, \quad (2.12)$$

where the variables  $f$  and  $g$  are called Lagrange coefficients, also known as the  $f$  and  $g$  functions. There are many ways to calculate the Lagrange coefficients, one of them being through the use of universal functions, which are used extensively throughout Ref. [4] and summarized in the equations to follow. The Lagrange coefficients in terms of universal functions are

$$f = 1 - \frac{U_2}{r_0}, \quad (2.13)$$

$$g = \frac{1}{\sqrt{\mu}}(r_0 U_1 + \sigma_0 U_2), \quad (2.14)$$

$$\dot{f} = -\frac{\sqrt{\mu} U_1}{r r_0}, \quad (2.15)$$

$$\dot{g} = 1 - \frac{U_2}{r}, \quad (2.16)$$

where

$$\sigma_0 = \frac{1}{\sqrt{\mu}}(\mathbf{r}_0 \cdot \mathbf{v}_0). \quad (2.17)$$

The universal functions are expressed differently whether the orbit is parabolic, hyperbolic, or elliptic. The expressions for the first four universal functions for elliptical orbits are

$$U_0 = \cos(\sqrt{z}\chi), \quad (2.18)$$

$$U_1 = \frac{\sin(\sqrt{z}\chi)}{\sqrt{z}}, \quad (2.19)$$

$$U_2 = \frac{1 - \cos(\sqrt{z}\chi)}{z}, \quad (2.20)$$

$$U_3 = \frac{\sqrt{z}\chi - \sin(\sqrt{z}\chi)}{z\sqrt{z}}, \quad (2.21)$$

where  $z$  is the reciprocal of the semi-major axis of the orbit and can be expressed as

$$z = \frac{2}{r_0} - \frac{v_0^2}{\mu}. \quad (2.22)$$

The variable  $\chi$  is an independent variable used instead of time, sometimes referred to as the generalized anomaly, and is related to the eccentric anomaly by

$$\chi = \sqrt{\frac{1}{z}}(E - E_0). \quad (2.23)$$

The universal functions are used to obtain the generalized form of Kepler's equation

$$\sqrt{\mu}(t - t_0) = r_0 U_1 + \sigma_0 U_2 + U_3. \quad (2.24)$$

If time is given, Eq. (2.24) must be solved for  $\chi$  to find the position in the orbit. This equation is transcendental in  $\chi$ , therefore an iterative scheme is necessary. Ref. [5] suggests using a first guess of

$$\chi_g = \sqrt{\mu} z(t-t_0), \quad (2.25)$$

where  $t$  is the time at which  $\mathbf{r}$  and  $\mathbf{v}$  are to be calculated and  $t_0 = 0$ . This guess is used in a Newton iteration algorithm

$$\chi_{g+1} = \chi_g + \frac{t - t_g}{\left. \frac{d\chi}{d\chi} \right|_{\chi=\chi_g}}, \quad (2.26)$$

where  $\chi_g$  is first used to calculate the universal functions and then Eq. (2.24) is used to calculate  $t_g$  by setting  $t = t_g$ . Substituting universal functions into Eq. (4.4-17) of Ref. [5] yields an expression for the term  $\frac{dt}{d\chi}$ , i.e.,

$$\frac{dt}{d\chi} = \frac{1}{\sqrt{\mu}} (r_0 U_0 + \sigma_0 U_1 + U_2). \quad (2.27)$$

Eq. (2.26) is iterated until  $t - t_g$  converges to the pre-assigned value.

## 2.4 Perturbing Forces

The solution to the two-body problem presented in the previous sections describes the relative motion between two particles when the only force acting on the particles is their mutual gravitation. In reality, other forces act on the bodies and perturb the motion. Some examples of these perturbing forces are gravitational forces from other bodies in the system

or the asphericity of the central body, atmospheric drag, electromagnetic forces due to interaction with magnetic fields, or solar radiation pressure. The additional forces and the deviations from two-body motion are called perturbations, and there are two methods for analyzing them. In the method of special perturbations, the equations of motion, including all perturbing accelerations, are numerically integrated. In the method of general perturbations, an analytical solution is achieved through variation of parameters. Both methods are described in Ref. [5]. The method of special perturbations will be used to include the perturbative effects due to comet outgassing on the two-body comet trajectories under study.

A comet is often thought of as a fuzzy point of light in the night sky. A comet appears “fuzzy” because the heat radiated from the Sun is sublimating the comet surface, and the evaporated materials form a cloud around the core, or nucleus, of the comet. The cloud of evaporated materials is called the coma. Solar radiation pressure and the solar wind blow this dust away from the nucleus and a tail is formed. The composition of the nucleus is still mostly unknown, but it is generally thought of as a “dirty snowball”. Based on spectroscopic observations of comet tails it has been speculated that the nucleus is made mostly of frozen water and organic and silicate compounds [6]. When the comet gets close enough to the Sun so that the materials in the nucleus begin to evaporate, the comet is said to be outgassing. This outgassing exerts forces on the comet that perturb the orbit, so it is necessary to determine whether the magnitude of these deviations will make it impossible to determine the orbit to some specified level of accuracy.

A commonly used method for modeling outgassing accelerations was developed by Marsden, Sekanina, and Yeomans, and is described in Ref. [7]. By carefully studying the

orbits of over 20 periodic comets they were able to derive the following expression for acceleration due to outgassing,

$$\boldsymbol{\alpha} = g(r)[A_1\hat{\mathbf{r}} + A_2\hat{\mathbf{t}} + A_3\hat{\mathbf{n}}], \quad (2.28)$$

where

$$g(r) = c \left( \frac{r}{r_0} \right)^{-m} \left[ 1 + \left( \frac{r}{r_0} \right)^n \right]^{-k}. \quad (2.29)$$

The unit vector  $\hat{\mathbf{r}}$  points in a direction parallel to the Sun-comet vector  $\mathbf{r}$  in the orbit plane,  $\hat{\mathbf{t}}$  is perpendicular to  $\mathbf{r}$  in the orbit plane, and  $\hat{\mathbf{n}}$  is perpendicular to the orbit plane. This model is based on the assumption that the comet is an “icy conglomerate” – an object consisting mostly of frozen water that holds together bits and pieces of rock-like material. This model also was used to generate accurate ephemerides for Halley’s comet [8]. In Eq. (2.29) the variable  $r$  is the heliocentric distance of the comet in AU, and all other parameters are constants based on studies of vaporization rates of comet nuclei materials and are derived in Ref. [7]. The constants are reported to be  $m = 2.15$ ,  $n = 5.093$ , and  $k = 4.6142$ . The normalizing constant  $c$  is defined such that  $g(1) = 1$ , and  $r_0$  is the scale heliocentric distance of high outgassing activity with a value equal to 2.808 AU for frozen water. Substituting these values into Eq. (2.29) and solving for the normalizing constant yields  $c = 0.1113$ . In Eq. (2.28),  $A_i$  ( $i = 1, 2, 3$ ) are constants describing the components of acceleration in the radial, transverse, and normal directions. Values of  $A_1$  and  $A_2$  calculated by studying changes in comet orbital periods are listed in Table I of Ref. [7] for various comets. Values for  $A_3$  are not given because the acceleration force normal to the orbit plane had no detectable effect on the orbital periods studied. However, a normal acceleration force may be present if the

comet is rotating or tumbling, and this component must be included in simulations designed to predict collisions. Without any given data for such a force it is assumed that  $A_3 = A_2$ . It should also be noted that the model is based on comets that have made multiple solar passes. A comet approaching the Sun for the first time may be subject to larger, or smaller, outgassing accelerations than described by this model, depending on the composition of the nucleus.

Before undertaking orbit determination simulations it is important to understand the magnitude of displacement from two-body motion along the comet trajectory caused by outgassing accelerations. These accelerations are included as an additional term in Eq. (2.10) so that the equation of motion for an outgassing comet is

$$\frac{d^2 \mathbf{r}}{dt^2} = -\frac{\mu}{r^3} \mathbf{r} + g(r) [A_1 \hat{\mathbf{r}} + A_2 \hat{\mathbf{T}} + A_3 \hat{\mathbf{n}}]. \quad (2.30)$$

By comparing results obtained through numerical integration of Eqs. (2.10) and (2.30), the perturbation to two-body motion caused by comet outgassing is determined as

$$\delta \mathbf{r}(t) = \mathbf{r}(t)_n - \mathbf{r}(t)_o, \quad (2.31)$$

where  $\mathbf{r}_n$  is the position of the comet calculated through integration of Eq. (2.10), and  $\mathbf{r}_o$  is the position calculated by integration of Eq. (2.30). The integration is performed for a sample long-period comet (orbital period greater than 200 years) on an Earth-impacting trajectory with orbital elements  $r_a = 300$  AU,  $r_p = 0.1$  AU,  $i = 45^\circ$ ,  $\Omega = 30^\circ$ ,  $\omega = 143.2^\circ$ , and  $v_0 = -163.9^\circ$  (criteria for creating such orbital elements is presented in Sec. 3). The orbital period for this comet is 1839.4 years. The equations of motion are integrated from  $t_0$  to  $t_f$ , corresponding to times when the comet is at heliocentric distances of 5 AU and 1 AU,

respectively. The maximum values for the acceleration coefficients listed in Ref. [7] are used for this analysis. These values are  $A_1 = 3.61 \text{ AU}/10^8 \text{ day}^2$  ( $5.4 \text{ km}/\text{day}^2$ ) and  $A_2 = A_3 = 0.3269 \text{ AU}/10^8 \text{ day}^2$  ( $0.49 \text{ km}/\text{day}^2$ ). Fig. 2 shows the absolute value of each component of  $\delta\mathbf{r}$ , denoted by  $\delta r_x$ ,  $\delta r_y$ , and  $\delta r_z$ , versus time on a logarithmic scale. Also shown is the magnitude of  $\delta\mathbf{r}$  versus time,  $\delta r$ , which is approximately 2,500 km by the time the comet reaches a heliocentric distance of 1 AU for this sample case. This deviation is sufficiently large compared to the size of the Earth that outgassing must be included in orbit determination accuracy calculations. However, the more important result is that the perturbations are less than 10 km until about 200 days, and can be considered negligible. At 200 days the comet has traveled to a heliocentric distance of about 2.5 AU. Since these deviations are so small compared to the heliocentric distance of the comet, a first order perturbation adequately

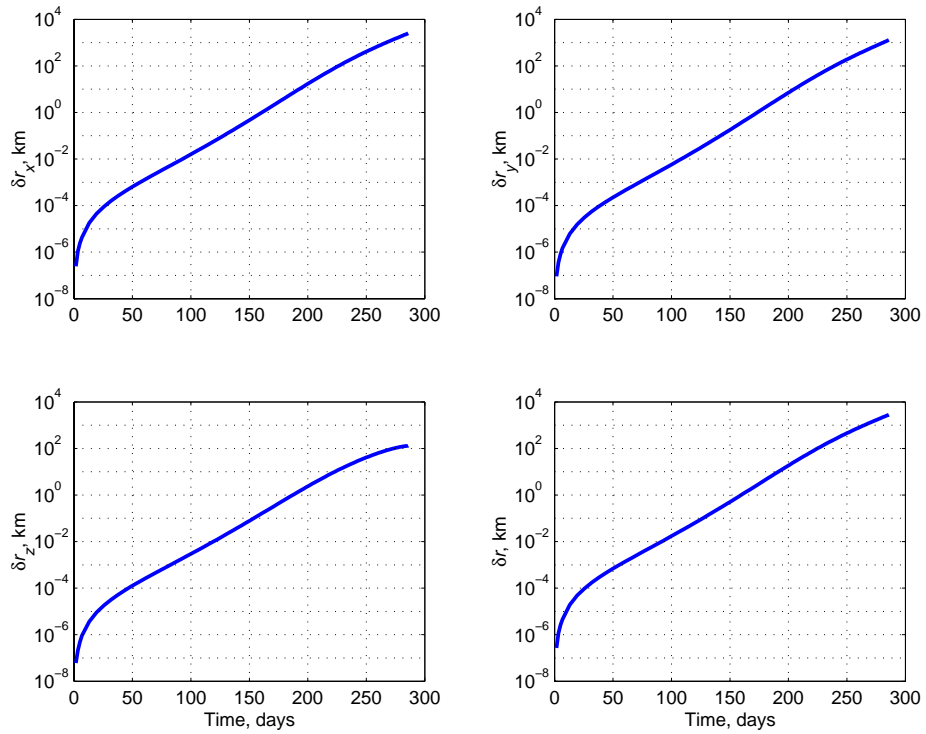


**Figure 2. Deviation in position due to outgassing forces for a long-period comet**

represents the motion of the comet, and a linear model is adequate to represent the perturbations for orbit determination purposes. This is confirmed through Monte Carlo simulations, the results of which are presented in Sec. 4.2.4.

A similar result is obtained for a short-period comet (orbital period less than 200 years) with orbital elements  $r_a = 40$  AU,  $r_p = 0.1$  AU,  $i = 50^\circ$ ,  $\Omega = 30^\circ$ ,  $\omega = 143.6^\circ$ , and  $\nu_0 = -164.8^\circ$ . The orbital period of this comet is 89.8 years. Fig. 3 also shows negligible perturbations until approximately 200 days, when the comet has reached a heliocentric distance of 2.6 AU.

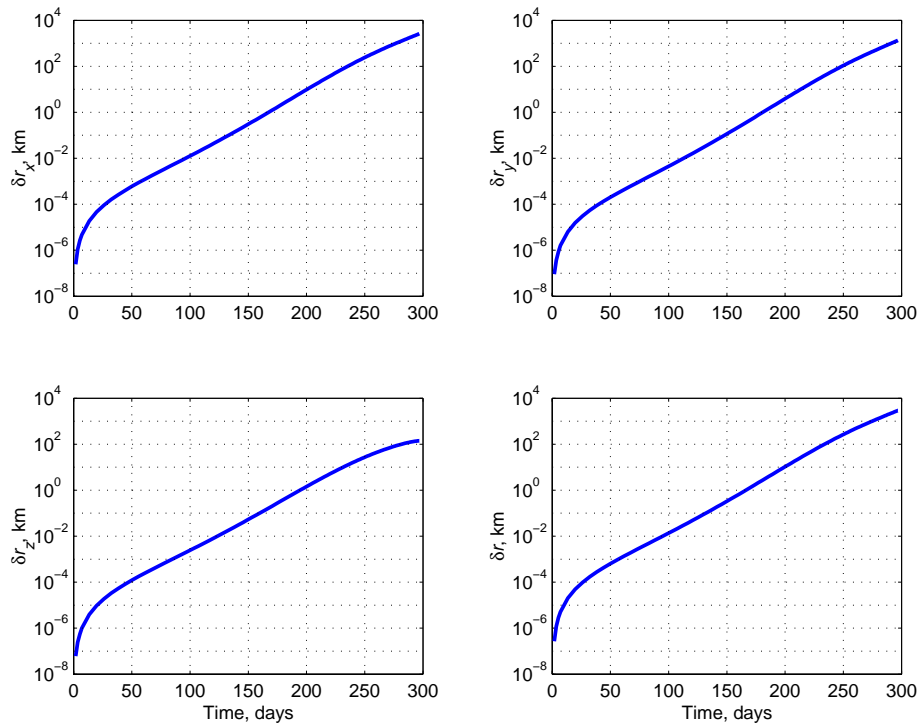


**Figure 3. Deviation in position due to outgassing forces for a short-period comet**

### **3 Impact Trajectory Criteria**

The accuracy of orbit determination depends on many factors. Some of these that are important to this investigation are the number of observations available, the time interval over which those observations are made, the resolution of the measuring device, and the geometry between the observatory and the object. A standard method for examining these effects is to construct a collision orbit, use this “reference” orbit to calculate a set of perfect measurements and add random noise to them, and then determine the “estimated” orbit using the noisy measurements with the orbit determination method described in Sec. 4. An important consideration in designing these true orbits is warning time. Warning time is the interval between the time when the comet orbit becomes known and the time of collision, and is greatly dependent on the heliocentric distance of the comet at the time observations are made. Warning time is discussed in Sec. 3.1, with the purpose of establishing an approximate distance at which the comet should be discovered to supply enough time to observe and determine the orbit to the desired degree of accuracy, while leaving roughly one year to plan and execute an evacuation scenario or even some type of mitigation technique. A set of comet orbits representing several different orbit geometries are designed to guarantee Earth-impact using the equations presented in Sec. 3.2 [9].

#### **3.1 Warning Time**

As stated previously, warning time is the interval between the time when the comet orbit becomes known with sufficient accuracy and the time when the collision takes place. It is possible that the comet will travel through several orbits in this time, but the possibility also exists that the comet will be discovered on its terminal orbit, greatly reducing the amount of



Inclination does not affect orbital period or the time of flight between one point and another; therefore, studying the coplanar case is suitable for generalizing warning time analysis. Perturbative effects on the comet due to the gravity of the Earth and comet outgassing are not considered in the analysis to follow, since these effects will not significantly change the time of flight on the relatively short time interval being investigated (compared to the orbital period of the comet).

The eccentric anomaly,  $E$ , at any point on an elliptic orbit is given by Eq. (A14). If  $E$  denotes the eccentric anomaly at the point of discovery where  $r$  is the distance between the Sun and the comet, and  $E_c$  denotes eccentric anomaly at the point of collision where  $r = r_c = 1$  AU, then the time of flight between these two points is calculated using Eq. (4.2-9) of Ref. [5] given here as

$$t - t_c = \sqrt{\frac{a^3}{\mu}} [(E - e \sin E) - (E_c - e \sin E_c)]. \quad (3.1)$$

Eq. (3.1) is used to calculate the warning times for a sample family of short- and long-period comets whose orbits become known at distances of 5, 6, and 7 AU. The family is constructed with perihelion distances,  $r_p$ , equal to 0.1 and 1 AU, and aphelion distances,  $r_a$ , equal to 15, 20, 25, ..., 100, 200, 300, ..., 1000, 2000, ...,  $50 \times 10^3$  AU. The range of orbital periods for these values of aphelia is between 20 years and  $4 \times 10^6$  years, reaching out to the middle of the Oort cloud. Long-period comets are typically defined as those with periods greater than 200 years.

Warning time as a function of  $r_a$  is displayed in Fig. 5. Warning time does not change significantly for aphelia greater than 1000 AU, and reducing  $r_p$  by a factor of 10 results in a loss of warning time by about the same amount as reducing the detection distance

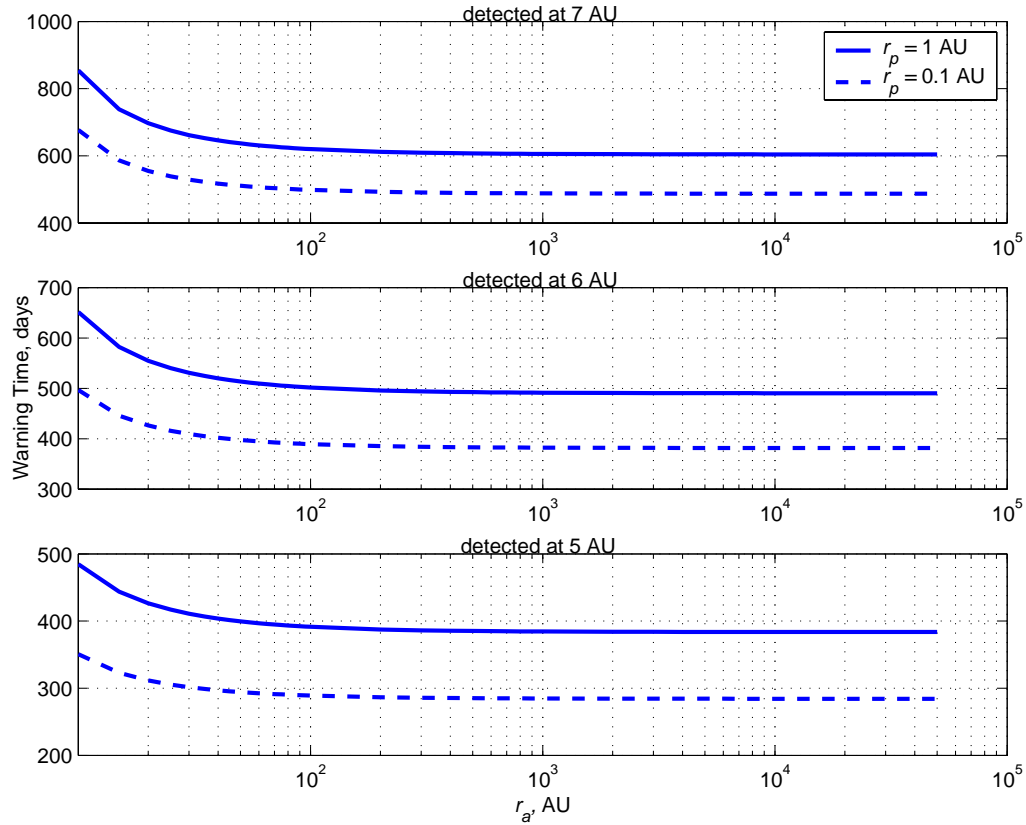


Figure 5. Times of flight between detection and collision for short- and long-period comets

by 1 AU. The range in warning times is between a little more than 2 years for the case where the comet is discovered at a distance of 7 AU, with  $r_p$  equal to 1 AU, and 9.5 months for the case where the comet is discovered at a distance of 5 AU, with  $r_p$  equal to 0.1 AU.

### 3.2 Designing Earth-Impacting Orbits

By design, all of the orbits to be studied pass through the ecliptic plane at a heliocentric distance of 1 AU. If the ecliptic plane is the reference plane, a comet in an inclined orbit is at the ascending or descending node when passing through the ecliptic. Therefore, the collision takes place when the comet is at the ascending or descending node, and the heliocentric

distance  $r$  is equal to  $r_c$ . Referring to Fig. A1, we see that  $\nu = -\omega$  when the object is located at ascending node, and  $\nu = \pi - \omega$  when the object is located at descending node. The equation of the orbit can be written in the form

$$r = \frac{r_p(1+e)}{1+e\cos\nu}, \quad (3.2)$$

which after substituting the collision requirements becomes

$$r_c = \frac{r_p(1+e)}{1 \pm e\cos\omega}, \quad (3.3)$$

where the positive and negative signs are associated with the ascending and descending nodes, respectively. Solving for argument of periapsis,  $\omega$ , gives

$$\pm \cos\omega = \frac{r_p}{r_c} \left( 1 + \frac{1}{e} \right) - \frac{1}{e}. \quad (3.4)$$

The comet orbit will intersect the orbit of the Earth as long as

$$r_p \leq r_c \quad (3.5)$$

and

$$r_c \leq r_a. \quad (3.6)$$

Therefore, Eq. (3.4) can be used to solve for the value of  $\omega$  that ensures a collision to take place at the ascending or descending node, as long as Eqs. (3.5) and (3.6) are satisfied. When the comet orbit lies in the ecliptic plane, the ascending and descending nodes will be undefined since  $i = 0^\circ$ . In this case, the value of  $\omega$  is arbitrary because a collision is ensured to occur as long as the conditions in Eqs. (3.5) and (3.6) are satisfied.

## 4 Orbit Determination and Collision Probability

It was shown in Sec. 2.2 that six parameters are necessary to define an orbit, either a set of six orbital elements or the six components of position and velocity. Therefore, a minimum set of six measurements is required to calculate an orbit, usually two angular measurements at three separate observation times. Newton was the first to describe a method for finding the orbit of a body from three observations, and Edmund Halley was the first person to apply this technique to the calculation of orbits. He used it to prove that a comet observed by Kepler in 1607 was the same comet he observed in 1682, and predicted that it would return in 1758. On Christmas day, 1758, the comet appeared in the night sky, fulfilling his prediction and ever after bearing his name [5].

Preliminary orbit determination is the process of using the minimum number of observations to calculate a first approximation of the six orbit parameters required to define an orbit. This approximation can then be combined with additional angular measurements, range information, and effects due to perturbative forces to obtain the orbit more precisely. The comet orbits under study have been designed to cross the ecliptic plane at a heliocentric distance of 1 AU where a collision at the center of the Earth is assumed to occur. The designed orbit defines a nominal set of observations consisting of celestial longitude,  $\varphi$ , celestial latitude,  $\lambda$ , and in some cases range,  $\rho$ , to which random noise is added to simulate observations collected from an observatory. The accuracy of the orbit determination can be quantified by comparing the orbits calculated with noisy measurements to the nominal orbit for different tracking schedules and observatory locations. Orbit determination methods are discussed in Sec. 4.1, and orbit determination accuracy is discussed in Sec. 4.2.

## 4.1 Methods of Orbit Determination

Ultimately it would be Gauss who would be remembered for solving the orbit determination problem based on three observations, although he knew himself that his method was only an approximation to be used for preliminary orbit determination. He's quoted as stating that improvement could only be made by accumulating "the greatest number of the most perfect observations, and to adjust the elements, not so as to satisfy this or that set of observations with absolute exactness, but so as to agree with all in the best possible manner" [5]. His method of weighted least squares is one way of combining a "great" number of observations to calculate an improved estimate of the orbit. This method usually employs observational data collected together as a "batch", and is applied to minimize the sum of the squares of the weighted residuals of the measurements. The batch process requires all data to be stored, so when a new measurement becomes available, it is added to the batch and the entire set is either reprocessed or augmented using a sequential batch process. Simple formulas exist for adding a new measurement without having to reprocess the entire data set, and various levels of importance can be placed on the measurements through weighting factors. However, the method of weighted least squares has no method for incorporating system noise to account for incomplete force modeling or measurement noise to account for imperfect observations. An orbit determination method that does incorporate system and measurement noise statistics makes use of the Kalman filter, a sequential data processing algorithm that yields a minimum error variance, or minimum trace of an error covariance matrix. This method is described in Sec. 4.1.2.

#### 4.1.1 Preliminary Orbit Determination Using Gauss' Method

Gauss' method makes use of measurements of longitude,  $\tilde{\varphi}$ , measured from vernal equinox in the ecliptic plane, and latitude,  $\tilde{\lambda}$ , measured from the ecliptic plane toward the north celestial pole. The *tilde* superscript denotes the fact that the measurements are assumed to have some error associated with them due to the measurement resolution of the observing device. Following the algorithm presented in Sec. 5.8 of Ref. [5], assuming that optical measurements  $\tilde{\varphi}$  and  $\tilde{\lambda}$  are available at three times  $t_1$ ,  $t_2$ , and  $t_3$ , a unit vector along the line of sight between the observatory and the comet is expressed as

$$\hat{\mathbf{L}}_i = (\cos \tilde{\varphi}_i \cos \tilde{\lambda}_i) \hat{i}_x + (\sin \tilde{\varphi}_i \cos \tilde{\lambda}_i) \hat{i}_y + (\sin \tilde{\lambda}_i) \hat{i}_z, \quad i = 1, 2, 3. \quad (4.1)$$

The heliocentric position of the comet can be expressed as

$$\mathbf{r} = \mathbf{d} + \hat{\mathbf{L}}\rho, \quad (4.2)$$

where  $\mathbf{d}$  is the heliocentric position of the observatory, and  $\rho$  is the magnitude of the distance between the observatory and the comet. If the vector  $\mathbf{r}(t)$  is expressed in terms of the Lagrange coefficients  $f$  and  $g$  at  $t_2$ , then

$$\mathbf{r}(t) = f(\mathbf{r}_2, \mathbf{v}_2, t - t_2) \mathbf{r}_2 + g(\mathbf{r}_2, \mathbf{v}_2, t - t_2) \mathbf{v}_2, \quad (4.3)$$

and with

$$f_i = f(\mathbf{r}_2, \mathbf{v}_2, t_i - t_2) \quad (4.4)$$

$$g_i = g(\mathbf{r}_2, \mathbf{v}_2, t_i - t_2), \quad (4.5)$$

a set of nine equations in the nine unknowns  $\mathbf{r}_2$ ,  $\mathbf{v}_2$ ,  $\rho_1$ ,  $\rho_2$ , and  $\rho_3$  can be expressed as

$$f_1 \mathbf{r}_2 + g_1 \mathbf{v}_2 = \mathbf{d}_1 + \rho_1 \mathbf{L}_1, \quad (4.6)$$

$$\mathbf{r}_2 = \mathbf{d}_2 + \rho_2 \mathbf{L}_2, \quad (4.7)$$

$$f_3 \mathbf{r}_2 + g_3 \mathbf{v}_2 = \mathbf{d}_3 + \rho_3 \mathbf{L}_3. \quad (4.8)$$

This set of equations is reduced to six independent equations in the six unknowns  $\mathbf{r}_2$  and  $\mathbf{v}_2$  by cross multiplying the  $i$ -th equation with  $\mathbf{L}_i$  and eliminating the  $\hat{i}_z$  components to obtain the following set of equations written in matrix notation,

$$\begin{bmatrix} f_1 L_{1,z} & 0 & -f_1 L_{1,x} & g_1 L_{1,z} & 0 & -g_1 L_{1,x} \\ 0 & f_1 L_{1,z} & -f_1 L_{1,y} & 0 & g_1 L_{1,z} & -g_1 L_{1,y} \\ L_{2,z} & 0 & -L_{2,x} & 0 & 0 & 0 \\ 0 & L_{2,z} & -L_{2,y} & 0 & 0 & 0 \\ f_3 L_{3,z} & 0 & -f_3 L_{3,x} & g_3 L_{3,z} & 0 & -g_3 L_{3,x} \\ 0 & f_3 L_{3,z} & -f_3 L_{3,y} & 0 & g_3 L_{3,z} & -g_3 L_{3,y} \end{bmatrix} \begin{bmatrix} r_x \\ r_y \\ r_z \\ v_x \\ v_y \\ v_z \end{bmatrix} = \begin{bmatrix} d_{1,x} L_{1,z} - d_{1,z} L_{1,x} \\ d_{1,y} L_{1,z} - d_{1,z} L_{1,y} \\ d_{2,x} L_{2,z} - d_{2,z} L_{2,x} \\ d_{2,y} L_{1,z} - d_{2,z} L_{2,y} \\ d_{3,x} L_{3,z} - d_{3,z} L_{3,x} \\ d_{3,y} L_{3,z} - d_{3,z} L_{3,y} \end{bmatrix}, \quad (4.9)$$

where  $r_x$ ,  $r_y$ , and  $r_z$  are the components of  $\mathbf{r}_2$ , and  $v_x$ ,  $v_y$ , and  $v_z$  are the components of  $\mathbf{v}_2$ . The variables  $f$  and  $g$  are functions of  $\mathbf{r}_2$  and  $\mathbf{v}_2$  and are obtained through the process outlined in Sec. 2.3. Eqs. (4.9) are nonlinear, and the procedure for solving this set of equations is as follows:

1. Estimate the vector  $\mathbf{r}_2$  using Eq. (4.2) at  $t_2$ , where  $\mathbf{d}_2$  and  $\mathbf{L}_2$  are known, and  $\rho_2$  is assigned a value of 5 AU (the distance at which the comet is assumed to be discovered);
2. Estimate the vector  $\mathbf{v}_2$  by forming the cross product of  $\mathbf{L}_1$  and  $\mathbf{L}_3$  to obtain a unit vector along the direction of the angular momentum,  $\hat{\mathbf{h}}$ ; form the cross product of  $\hat{\mathbf{h}}$

with a unit vector in the direction of the estimated position,  $\hat{\mathbf{r}}_2$ , to obtain a unit vector in the direction of the estimated velocity,  $\hat{\mathbf{v}}_2$ ; estimate the magnitude of  $\mathbf{v}_2$  using the expression for circular velocity, i.e.,

$$v_2 = \sqrt{\frac{\mu}{r_2}};$$

3. Using these estimates, compute the values of  $f_1$ ,  $g_1$ ,  $f_2$ , and  $g_2$  using the equations presented in Sec. 2.3, and substitute into Eq. (4.9) to solve for the components of  $\mathbf{r}_2$  and  $\mathbf{v}_2$ ;
4. Update  $f_1$ ,  $g_1$ ,  $f_2$ , and  $g_2$  and iterate until  $\mathbf{r}_2$  and  $\mathbf{v}_2$  converge.

In all of the analysis to follow, Gauss' method is used with three observations spaced seven days apart to determine preliminary orbits and other required initial parameters for the Kalman filter. The preliminary orbit serves as an initial guess for the filter, and additional observations are collected to attain more accurate orbit determination.

#### **4.1.2 Final Orbit Determination Using the Kalman Filter**

As previously stated, the Kalman filter is a sequential filter, or a recursive data processing algorithm in which an estimate of the state, namely the six components of position and velocity, determined from measurement data available at the current time is updated when measurements become available at subsequent times. The objective of any type of filter is to obtain this estimate while minimizing the error in some respect. The Kalman filter is an optimal estimator that minimizes the error variance, or the trace of the error covariance matrix. The Kalman filter can incorporate all available measurements and measurement uncertainties, along with the dynamics models of the comet and observatory and the

uncertainty in these models to produce an estimate of comet position and velocity at the time of each observation.

#### 4.1.2.1 State Propagation

Using a Kalman filter requires some basic assumptions to be made about the problem. First, the problem must be described using a linear model. Since the orbit determination problem is nonlinear, the approach is to linearize about a reference trajectory. Let  $\mathbf{r}^*(t)$  and  $\mathbf{v}^*(t)$  be the position and velocity of the comet on the reference trajectory. The comet will not follow this reference trajectory exactly, and the actual position,  $\mathbf{r}(t)$ , and velocity,  $\mathbf{v}(t)$ , will deviate from  $\mathbf{r}^*(t)$  and  $\mathbf{v}^*(t)$ . Expanding  $\mathbf{r}(t)$  and  $\mathbf{v}(t)$  in a Taylor series about the reference trajectory yields

$$\mathbf{r}(t) = \mathbf{r}^*(t) + \left[ \frac{\partial \mathbf{r}(t)}{\partial \mathbf{r}(t_0)} \right]^* \delta \mathbf{r}_0 + \left[ \frac{\partial \mathbf{r}(t)}{\partial \mathbf{v}(t_0)} \right]^* \delta \mathbf{v}_0 + \dots, \quad (4.10)$$

$$\mathbf{v}(t) = \mathbf{v}^*(t) + \left[ \frac{\partial \mathbf{v}(t)}{\partial \mathbf{r}(t_0)} \right]^* \delta \mathbf{r}_0 + \left[ \frac{\partial \mathbf{v}(t)}{\partial \mathbf{v}(t_0)} \right]^* \delta \mathbf{v}_0 + \dots, \quad (4.11)$$

where  $[ ]^*$  indicates that the matrix of partial derivatives is evaluated on the reference trajectory, higher order terms are neglected, and

$$\delta \mathbf{r}_0 = \mathbf{r}(t_0) - \mathbf{r}^*(t_0), \quad (4.12)$$

$$\delta \mathbf{v}_0 = \mathbf{v}(t_0) - \mathbf{v}^*(t_0). \quad (4.13)$$

If a state deviation vector  $\mathbf{x}$  is defined as

$$\mathbf{x}(t) = \begin{bmatrix} \delta \mathbf{r}(t) \\ \delta \mathbf{v}(t) \end{bmatrix}, \quad (4.14)$$

then Eqs. (4.10) and (4.11) can be written as

$$\mathbf{x}(t) = \Phi(t, t_0)\mathbf{x}(t_0) + \mathbf{w}(t_0), \quad (4.15)$$

where  $\Phi(t, t_0)$  is the state transition matrix, given by

$$\Phi(t, t_0) = \left[ \begin{array}{cc} \frac{\partial \mathbf{r}(t)}{\partial \mathbf{r}(t_0)} & \frac{\partial \mathbf{r}(t)}{\partial \mathbf{v}(t_0)} \\ \frac{\partial \mathbf{v}(t)}{\partial \mathbf{r}(t_0)} & \frac{\partial \mathbf{v}(t)}{\partial \mathbf{v}(t_0)} \end{array} \right]^*. \quad (4.16)$$

As before, [ ]<sup>\*</sup> indicates that the matrix of partial derivatives is evaluated on the reference trajectory. The numerical values of the elements populating  $\Phi$  can be calculated from the analytical expressions of Eqs. (9.84) through (9.87) in Ref. [4], which are repeated below,

$$\frac{\partial \mathbf{r}}{\partial \mathbf{r}_0} = \frac{r}{\mu} (\mathbf{v} - \mathbf{v}_0)(\mathbf{v} - \mathbf{v}_0)^T + \frac{1}{r_0^3} [r_0(1-f) \mathbf{r}\mathbf{r}_0^T + C\mathbf{v}\mathbf{r}_0^T] + f\mathbf{I} \quad (4.17)$$

$$\frac{\partial \mathbf{r}}{\partial \mathbf{v}_0} = \frac{r_0}{\mu} (1-f) [(\mathbf{r} - \mathbf{r}_0) \mathbf{v}_0^T - (\mathbf{v} - \mathbf{v}_0) \mathbf{r}_0^T] + \frac{C}{\mu} \mathbf{v}\mathbf{v}_0^T + g\mathbf{I} \quad (4.18)$$

$$\begin{aligned} \frac{\partial \mathbf{v}}{\partial \mathbf{r}_0} = & -\frac{1}{r_0^2} (\mathbf{v} - \mathbf{v}_0) \mathbf{r}_0^T - \frac{1}{r^2} \mathbf{r}(\mathbf{v} - \mathbf{v}_0)^T \\ & + f \left[ \mathbf{I} - \frac{1}{r^2} \mathbf{r}\mathbf{r}^T + \frac{1}{\mu r} (\mathbf{r}\mathbf{v}^T - \mathbf{v}\mathbf{r}^T) \mathbf{r}(\mathbf{v} - \mathbf{v}_0)^T \right] - \frac{\mu C}{r^3 r_0^3} \mathbf{r}\mathbf{r}_0^T \end{aligned} \quad (4.19)$$

$$\frac{\partial \mathbf{v}}{\partial \mathbf{v}_0} = \frac{r_0}{\mu} (\mathbf{v} - \mathbf{v}_0)(\mathbf{v} - \mathbf{v}_0)^T + \frac{1}{r^3} [r_0(1-f) \mathbf{r}\mathbf{r}_0^T - C\mathbf{r}\mathbf{v}_0^T] + g\mathbf{I}, \quad (4.20)$$

where  $C$  is introduced for convenience of notation and is defined in terms of universal variables by

$$C = \frac{1}{\sqrt{\mu}}(3U_5 - \chi U_4) - (t - t_0) U_2. \quad (4.21)$$

The quantity  $C$  is determined using the equations given in Sec. 2.3, along with the following expressions for the universal variables  $U_4$  and  $U_5$ ,

$$U_4 = U_1 U_3 - \frac{1}{2}(U_2^2 - z U_3^2), \quad (4.22)$$

$$U_5 = \frac{1}{U_1 - \chi} \left( U_3^2 - \frac{1}{6} \chi^3 U_3 \right). \quad (4.23)$$

When  $\chi = U_1 = 0$ , it can be shown through identities given in Ref. [4] that  $U_5 = 0$ .

#### 4.1.2.2 The Observation Equation

The observations are assumed to occur at discrete points in time and follow the linear relation

$$\mathbf{y}_k = \tilde{\mathbf{H}}_k \mathbf{x}_k + \boldsymbol{\epsilon}_k, \quad (4.24)$$

where the subscript  $k$  denotes the discrete point in time,  $t_k$ . The vector  $\mathbf{y}_k$  is an  $m \times 1$  observation residual vector, the elements of which are the difference between the measurements on the actual trajectory and the measurements on the reference trajectory, and  $\boldsymbol{\epsilon}_k$  are the errors in the measurements. The matrix  $\tilde{\mathbf{H}}$  is an  $m \times 6$  matrix of partial derivatives of the observations with respect to the state vector, where the state vector is a 6-dimensional column vector of the components of position and velocity at time  $t_k$ . This matrix is generally based on the geometry of the problem and is sometimes referred to as the observation matrix.

For measurements of longitude and latitude, the observation matrix is expressed as

$$\tilde{\mathbf{H}} = \begin{bmatrix} \frac{-\rho_y}{(\rho_x^2 + \rho_y^2)} & \frac{\rho_x}{(\rho_x^2 + \rho_y^2)} & 0 & 0 & 0 & 0 \\ \frac{-\rho_x \rho_z}{\rho^2 (\rho_x^2 + \rho_y^2)^{1/2}} & \frac{-\rho_y \rho_z}{\rho^2 (\rho_x^2 + \rho_y^2)^{1/2}} & \frac{(\rho_x^2 + \rho_y^2)^{1/2}}{\rho^2} & 0 & 0 & 0 \end{bmatrix}^*, \quad (4.25)$$

where  $\boldsymbol{\rho}$  is the position vector of the comet with respect to the observatory, i.e.,

$$\boldsymbol{\rho} = \rho_x \hat{i}_x + \rho_y \hat{i}_y + \rho_z \hat{i}_z, \quad (4.26)$$

and  $\rho$  is the magnitude of  $\boldsymbol{\rho}$ . When each observation consists of two angular measurements, the dimension of  $\mathbf{y}_k$  is  $2 \times 1$  and the dimension of  $\tilde{\mathbf{H}}$  is  $2 \times 6$ ; if a measurement of range is added to each observation, the dimension of  $\mathbf{y}_k$  is  $3 \times 1$  and the dimension of  $\tilde{\mathbf{H}}$  is  $3 \times 6$ . The first two rows of  $\tilde{\mathbf{H}}$  will be the same as above, and the last row will contain the partial derivatives of the measurement of range with respect to the state, i.e.,

$$\left[ \frac{\partial \rho}{\partial \mathbf{X}} \right]^* = \begin{bmatrix} \frac{\rho_x}{\rho} & \frac{\rho_y}{\rho} & \frac{\rho_z}{\rho} & 0 & 0 & 0 \end{bmatrix}^*. \quad (4.27)$$

The second Kalman filter assumption is that the measurement noises are white, meaning the values of noise are not correlated in time. In other words, the value of noise at a particular time cannot be predicted based on knowledge of the noise value at previous times. Therefore, the measurement errors  $\boldsymbol{\epsilon}_k$  in Eq. (4.24) are uncorrelated errors with

$$\begin{aligned} E\{ \boldsymbol{\epsilon}(t) \} &= 0 \\ E\{ \boldsymbol{\epsilon}(t) \boldsymbol{\epsilon}(t)^T \} &= \mathbf{R}(t), \end{aligned} \quad (4.28)$$

where the  $m \times m$  matrix  $\mathbf{R}(t)$  is the covariance of  $\boldsymbol{\varepsilon}$  and describes the uncertainty in the observations.

#### 4.1.2.3 Time and Measurement Updates

The initial state deviation  $\mathbf{x}(t_0)$  will not be known precisely *a priori*. Therefore, the dynamics model of Eq. (4.15) is written in terms of an estimate of the initial state deviation  $\hat{\mathbf{x}}(t_0)$ , i.e.,

$$\hat{\mathbf{x}}(t) = \Phi(t, t_0) \hat{\mathbf{x}}(t_0) + \mathbf{w}(t_0), \quad (4.29)$$

where  $\mathbf{w}(t_0)$  is white noise with

$$\begin{aligned} E\{ \mathbf{w}(t) \} &= 0 \\ E\{ \mathbf{w}(t) \mathbf{w}(t)^\top \} &= \mathbf{Q}(t). \end{aligned} \quad (4.30)$$

The  $6 \times 6$  matrix  $\mathbf{Q}(t)$  is the covariance of  $\mathbf{w}$  and describes the uncertainty in the dynamics model. A  $6 \times 6$  covariance matrix  $\mathbf{P}$  is defined in terms of the error in the estimate of the state deviation vector,

$$E\{ [\mathbf{x}(t) - \hat{\mathbf{x}}(t)] [\mathbf{x}(t) - \hat{\mathbf{x}}(t)]^\top \} = \mathbf{P}. \quad (4.31)$$

The Kalman filter is used to estimate and update the state deviation vector from the time when one measurement is processed,  $t_{k-1}$ , to the time the next measurement is processed,  $t_k$ . This process can be thought of as consisting of two parts: a time update and a measurement update. The procedure uses the solution at time  $t_{k-1}$  as the starting point for the update at time  $t_k$ . Consider the state deviation at a time just after a measurement update,

denoted by  $t_{k-1}^+$ , and a time just before the next measurement update,  $t_k^-$ . The time updates of the state deviation vector and the covariance matrix  $\mathbf{P}$  are given by Eqs. (4.2-17) and (4.2-18) in Ref. [10] repeated here,

$$\hat{\mathbf{x}}_k^- = \Phi(t_k, t_{k-1}) \hat{\mathbf{x}}_{k-1}^+, \quad (4.32)$$

$$\mathbf{P}_k^- = \Phi(t_k, t_{k-1}) \mathbf{P}_{k-1}^+ \Phi(t_k, t_{k-1})^T + \mathbf{Q}_{k-1}. \quad (4.33)$$

The measurement updates of the state deviation vector and the covariance matrix  $\mathbf{P}$  are given by Eqs. (4.2-5) and (4.2-12) in Ref. [10] as

$$\hat{\mathbf{x}}_k^+ = \hat{\mathbf{x}}_k^- + \mathbf{K}_k [\mathbf{y}_k - \tilde{\mathbf{H}}_k \hat{\mathbf{x}}_k^-], \quad (4.34)$$

$$\mathbf{P}_k^+ = (\mathbf{I} - \mathbf{K}_k \tilde{\mathbf{H}}_k) \mathbf{P}_k^- (\mathbf{I} - \mathbf{K}_k \tilde{\mathbf{H}}_k)^T + \mathbf{K}_k \mathbf{R}_k \mathbf{K}_k^T, \quad (4.35)$$

where  $\mathbf{K}$  is the Kalman gain, given by Eq. (4.2-15) in Ref. [10] as,

$$\mathbf{K}_k = \mathbf{P}_k^- \tilde{\mathbf{H}}_k^T [\tilde{\mathbf{H}}_k \mathbf{P}_k^- \tilde{\mathbf{H}}_k^T + \mathbf{R}_k]^{-1}, \quad (4.36)$$

and is an optimal gain matrix that weights the measurements more heavily if  $\mathbf{K}$  is large and less heavily if  $\mathbf{K}$  is small.

The filter generates the best prediction of the state deviation  $\hat{\mathbf{x}}_k^-$  at time  $t_k$  before the measurement at time  $t_k$  is processed, and generates the best prediction  $\tilde{\mathbf{H}}_k \hat{\mathbf{x}}_k^-$  of what the measurement deviation will be before the measurement is actually taken. The measurement residual is calculated as the difference between the measurement deviation  $\mathbf{y}_k$  and  $\tilde{\mathbf{H}}_k \hat{\mathbf{x}}_k^-$ , and then multiplied by the gain matrix,  $\mathbf{K}_k$ , to produce a correction term to be added to  $\hat{\mathbf{x}}_k^-$  to

obtain  $\hat{\mathbf{x}}_k^+$ . This correction term is proportional to both  $\mathbf{K}_k$  and the measurement residual  $[\mathbf{y}_k - \tilde{\mathbf{H}}_k \hat{\mathbf{x}}_k^-]$ . The algorithm has a predictor-corrector structure. The Kalman filter algorithm is completely defined by specifying  $\Phi$  and  $\tilde{\mathbf{H}}$  for all times of interest, and supplying  $\hat{\mathbf{x}}(t_0)$ ,  $\mathbf{y}_k$ , and the uncertainties  $\mathbf{P}_0$ ,  $\mathbf{Q}(t)$ , and  $\mathbf{R}(t)$  [11].

An initial estimate of the state deviation  $\hat{\mathbf{x}}(t_0)$  is supplied in the form of a 6×1 column vector of deviations in position and velocity from the true comet orbit, and a corresponding initial 6×6 covariance matrix  $\mathbf{P}_0$  describing the uncertainties in  $\hat{\mathbf{x}}(t_0)$ . The initial conditions are obtained from a preliminary orbit determined by Gauss' method, using three observations collected by an observatory with measurement resolution  $\eta$  equal to 0.1 arcseconds (comparable to Hubble Space Telescope). The Gauss algorithm presented in Sec. 4.1.1 is used 100 times with 100 sets of six observations that have normally distributed noise with zero mean and standard deviation equal to  $\eta$ . The samples are truncated at  $\pm 2\eta$ . From this process, 100 different preliminary orbit solutions are obtained. The initial estimate of the state deviation,  $\hat{\mathbf{x}}(t_0)$ , is the difference between the Gauss solution and the designed orbit. The initial covariance matrix is calculated from the 100 state deviation vectors.

Since outgassing forces have been shown to be negligible during the time interval when observations are being collected, all time updates are performed by way of the two-body state transition matrix of Eq. (4.16). Comet outgassing introduces an uncertainty in the two-body assumption and is modeled as two effects – a varying uncertainty that changes with time and a constant uncertainty that acts over the entire orbit. The time-varying uncertainty is modeled as white state noise with zero mean and diagonal covariance  $\mathbf{Q}(t)$ . The elements of  $\mathbf{Q}(t)$  are calculated with the aid of Eq. (2.28). Since it is impossible to know ahead of time the values of the outgassing coefficients for a newly discovered comet, a distribution of

values between the maximum and minimum values of  $A_i$  ( $i = 1, 2, 3$ ) given in Ref. [7] is used to determine standard deviations for the coefficients,  $\sigma_{A_i}$  ( $i = 1, 2, 3$ ). Using the  $\sigma_{A_i}$  ( $i = 1, 2, 3$ ) in place of the  $A_i$  ( $i = 1, 2, 3$ ) in Eq. (2.28), outgassing acceleration  $\boldsymbol{\alpha}'$  is determined. Assuming  $\boldsymbol{\alpha}'$  is constant over the time interval between observations, the deviation in position due to outgassing acceleration is expressed as

$$\delta \mathbf{r} = \frac{1}{2} \boldsymbol{\alpha}' (t_k - t_{k-1})^2, \quad (4.37)$$

and the deviation in velocity is expressed as

$$\delta \mathbf{v} = \boldsymbol{\alpha}' (t_k - t_{k-1}), \quad (4.38)$$

where the quantity  $(t_k - t_{k-1})$  is the time interval between observations. The uncertainty in the system model can be expressed as

$$\mathbf{Q}_{ii}(t_k) = \delta r_i^2, \quad i = 1, 2, 3 \quad (4.39)$$

$$\mathbf{Q}_{ii}(t_k) = \delta v_{i-3}^2, \quad i = 4, 5, 6. \quad (4.40)$$

The constant element of uncertainty caused by outgassing is described in Sec. 4.2.2.

## 4.2 Orbit Determination Accuracy

Body plane (B-plane) targeting is a method commonly used for determining spacecraft closest approach distance to a target planet during the design phase of interplanetary missions, and for interplanetary orbit determination and maneuver targeting. This method is

easily applied to define a metric to quantify orbit determination accuracy for Earth-impacting comets in terms of miss distance. Results from B-plane analysis can be used further to determine Earth collision probability, as in Ref. [12].

#### 4.2.1 The B-plane

The B-plane is defined as a plane passing through the center of the target planet, perpendicular to the asymptote of the incoming hyperbolic orbit. The vector  $\mathbf{B}$  is a vector in that plane, on a line from the center of the target planet to the point where the asymptote intersects the plane, as shown in Fig. 6. The vector  $\mathbf{B}$  determines where the point of closest approach would be assuming the target planet had no mass and did not influence the

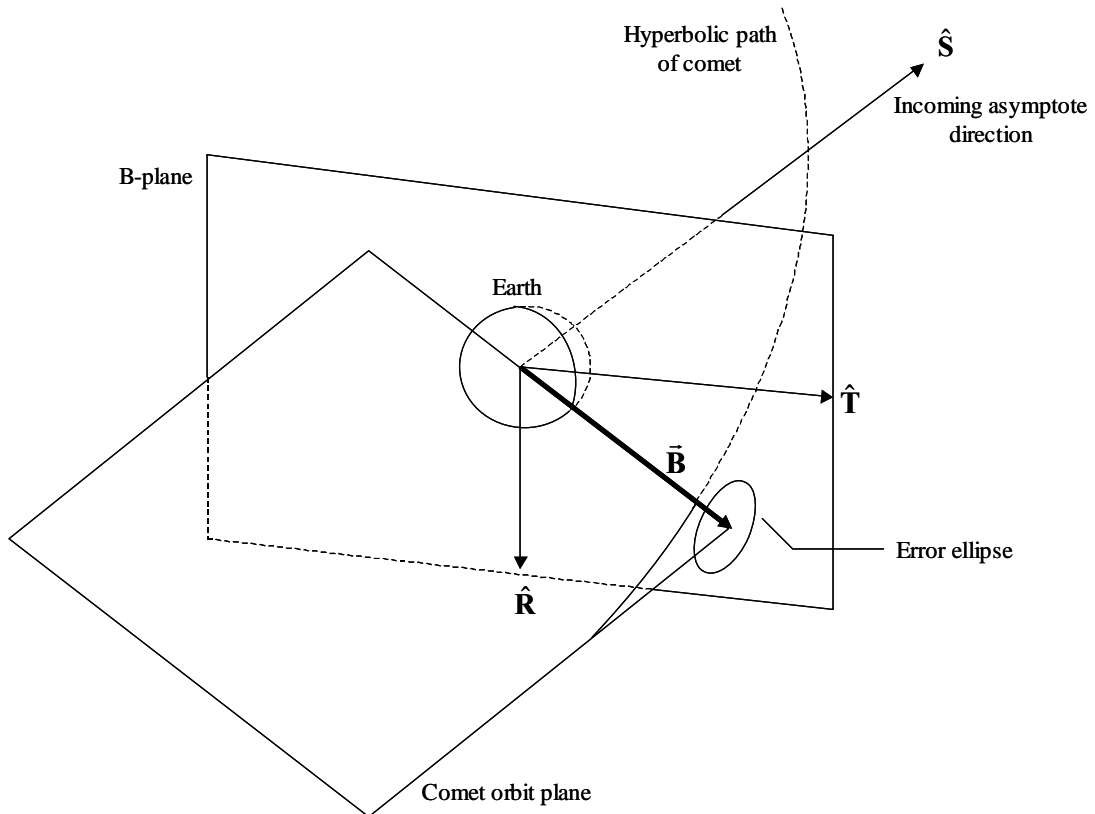


Figure 6. B-plane geometry

trajectory. A coordinate system with origin at the center of the target planet is defined by three orthogonal unit vectors  $\hat{\mathbf{T}}$ ,  $\hat{\mathbf{R}}$ , and  $\hat{\mathbf{S}}$ . The unit vector  $\hat{\mathbf{S}}$  points in the direction parallel to the incoming asymptote,  $\hat{\mathbf{T}}$  is normal to  $\hat{\mathbf{S}}$  and lies in the ecliptic plane, and  $\hat{\mathbf{R}}$  completes the orthogonal basis. The construction of the basis is such that  $\hat{\mathbf{S}}$  is perpendicular to the B-plane, and  $\hat{\mathbf{T}}$  and  $\hat{\mathbf{R}}$  lie within it.

In the present study, the B-plane is constructed with the Earth as the target planet. Ignoring the gravity of the Earth, the velocity at infinity can be calculated as

$$\mathbf{v}_\infty = \mathbf{v}_C(t_c) - \mathbf{v}_E(t_c), \quad (4.41)$$

where  $\mathbf{v}_C(t_c)$  and  $\mathbf{v}_E(t_c)$  are the velocities of the comet and the Earth in the inertial reference frame at the designed time of collision, respectively. Thus,

$$\hat{\mathbf{S}} = \frac{\mathbf{v}_\infty}{v_\infty}. \quad (4.42)$$

The unit vector  $\hat{\mathbf{T}}$  lies in the ecliptic plane perpendicular to  $\hat{\mathbf{S}}$ , therefore

$$\hat{\mathbf{T}} = \frac{\hat{\mathbf{S}} \times \hat{i}_z}{\|\hat{\mathbf{S}} \times \hat{i}_z\|}. \quad (4.43)$$

The unit vector  $\hat{\mathbf{R}}$  is

$$\hat{\mathbf{R}} = \hat{\mathbf{S}} \times \hat{\mathbf{T}}. \quad (4.44)$$

As stated previously, the vector  $\mathbf{B}$  is a vector in the B-plane, extending from the center of the Earth to the point where the hyperbolic asymptote intersects the B-plane. Since

$\hat{\mathbf{S}}$  is normal to the B-plane, and since both  $\mathbf{B}$  and  $\hat{\mathbf{S}}$  lie in the trajectory plane,  $\mathbf{B}$  must satisfy the expressions

$$\mathbf{B} \times (v_\infty \hat{\mathbf{S}}) = \mathbf{h}, \quad (4.45)$$

$$\mathbf{B} \cdot (v_\infty \hat{\mathbf{S}}) = 0, \quad (4.46)$$

where  $\mathbf{h}$  is the angular momentum of the comet relative to the center of the Earth,

$$\mathbf{h} = \mathbf{r}_\infty \times \mathbf{v}_\infty, \quad (4.47)$$

and  $\mathbf{r}_\infty$  is the relative position of the comet with respect to the Earth at the designed time of collision,

$$\mathbf{r}_\infty = \mathbf{r}_C(t_c) - \mathbf{r}_E(t_c). \quad (4.48)$$

Forming the cross product of  $\hat{\mathbf{S}}$  with Eq. (4.45) gives

$$\hat{\mathbf{S}} \times (\mathbf{B} \times \hat{\mathbf{S}}) = \frac{1}{v_\infty} (\hat{\mathbf{S}} \times \mathbf{h}), \quad (4.49)$$

or

$$(\hat{\mathbf{S}} \cdot \hat{\mathbf{S}}) \mathbf{B} - (\hat{\mathbf{S}} \cdot \mathbf{B}) \hat{\mathbf{S}} = \frac{1}{v_\infty} (\hat{\mathbf{S}} \times \mathbf{h}). \quad (4.50)$$

Since  $\hat{\mathbf{S}}$  is a unit vector, and since  $\mathbf{B}$  and  $\hat{\mathbf{S}}$  are mutually orthogonal, Eq. (4.50) becomes

$$\mathbf{B} = \frac{1}{v_\infty} (\hat{\mathbf{S}} \times \mathbf{h}). \quad (4.51)$$

The magnitude of  $\mathbf{B}$  is the miss distance. It is common to describe  $\mathbf{B}$  using the two components along the  $\hat{\mathbf{T}}$  and  $\hat{\mathbf{R}}$  directions,

$$B_T = \mathbf{B} \cdot \hat{\mathbf{T}}, \quad (4.52)$$

$$B_R = \mathbf{B} \cdot \hat{\mathbf{R}}, \quad (4.53)$$

and describe them verbally as “B dot T” and “B dot R”.

#### 4.2.2 State Uncertainties at Nominal Collision Time

A collision occurs at the center of the Earth by design. Therefore, if the collected observations were perfect, producing perfect orbit determination,  $\mathbf{B}$  would be zero. Of course, the observations have random noise associated with them and a perfectly determined orbit is not expected. The objective of the Kalman filter process is to determine a vector  $\mathbf{B}$  and an associated uncertainty. This uncertainty is determined by propagating the final Kalman covariance matrix  $\mathbf{P}_k^+$  from  $t_k$  to  $t_c$  by

$$\mathbf{P}_c = \Phi(t_c, t_k) \mathbf{P}_k^+ \Phi(t_c, t_k)^T + \mathbf{Q}_k, \quad (4.54)$$

with a modification required for the calculation of  $\mathbf{Q}_k$ . The state noise covariance given in Eqs. (4.39) and (4.40) is valid for short time intervals over which outgassing forces are assumed constant. The interval between the time of the last observation and the designed time of collision is too long for this assumption to remain valid (approximately one year), so this long interval is divided into 20 shorter intervals (each roughly two weeks). The modified time update is

$$\mathbf{P}_{k+1} = \Phi(t_{k+1}, t_k) \mathbf{P}_k^+ \Phi(t_{k+1}, t_k)^T + \overline{\mathbf{Q}}_k, \quad (4.55)$$

where  $\overline{\mathbf{Q}}_k$  is the average state noise covariance for the shorter time interval,

$$\overline{\mathbf{Q}}_k = \frac{\mathbf{Q}_k + \mathbf{Q}_{k+1}}{2}. \quad (4.56)$$

Eqs. (4.55) and (4.56) are applied repeatedly until  $t_{k+1} = t_c$ . The covariance matrix  $\mathbf{P}_c$  is a 6×6 matrix describing the uncertainty in the Kalman filter solution at the designed time of collision. However, only the upper left 3×3 partition of  $\mathbf{P}_c$  is of interest, since this partition contains uncertainties in position, and is denoted by  $\hat{\mathbf{P}}_c$ . As mentioned previously, uncertainty due to comet outgassing is modeled as two effects. The time varying uncertainty is contained in the covariance  $\mathbf{Q}(t)$  as described above. The constant uncertainty is included by supplementing  $\hat{\mathbf{P}}_c$  with a covariance matrix calculated from differences in position at the designed time of collision caused by outgassing. Eq. (2.28) is numerically integrated from the time of the first observation to the designed time of collision,  $t_c$ , once with  $\boldsymbol{\alpha} = 0$ , and then three times, each with  $\boldsymbol{\alpha}$  calculated using one of the  $\sigma_{A_i}$  ( $i = 1, 2, 3$ ) previously introduced. The difference in  $\mathbf{r}(t_k)$  between the  $\boldsymbol{\alpha} = 0$  and  $\sigma_{A_i}$  solutions are expressed as a 3×1 column matrix,  $\boldsymbol{\delta}$ , and the supplemented covariance matrix is

$$\bar{\mathbf{P}}_c = \hat{\mathbf{P}}_c + \sum_{i=1}^3 \boldsymbol{\delta}_i \boldsymbol{\delta}_i^T . \quad (4.57)$$

### 4.2.3 Position Uncertainty in the B-plane

The covariance given by Eq. (4.57) is associated with unit vectors in the inertial coordinate frame, and therefore must be rotated to the B-plane coordinate frame. If  $\mathbf{C}$  denotes the direction cosine matrix required for the rotation, then the covariance matrix in the B-plane coordinate frame is given by

$$\mathbf{P}_B = \mathbf{C} \bar{\mathbf{P}}_c \mathbf{C}^T . \quad (4.58)$$

The uncertainty in the orbit solution can be thought of as a 3-dimensional error ellipsoid centered at the B-plane intersection point marked by the vector  $\mathbf{B}$ . The error in position is described by a 2-dimensional ellipse formed by the intersection of this ellipsoid with the B-plane, and is determined from the  $2 \times 2$  partition of  $\mathbf{P}_B$  associated with the unit vectors  $\hat{\mathbf{T}}$  and  $\hat{\mathbf{R}}$ . This  $2 \times 2$  partition is denoted by  $\mathbf{P}_b$ . The semimajor and semiminor axes of the error ellipse, denoted by  $\sigma_1$  and  $\sigma_2$  respectively, are the square roots of the eigenvalues of  $\mathbf{P}_b$ . The eigenvalues are the elements of a diagonal matrix  $\mathbf{D}$  given by

$$\mathbf{D} = \mathbf{V}^T \mathbf{P}_b \mathbf{V}, \quad (4.59)$$

where  $\mathbf{V}$  is a matrix containing the normalized eigenvectors whose directions are parallel to the principal axes of the error ellipse. The orientation of the error ellipse is

$$\theta = \tan^{-1} \left( \frac{\mathbf{V}_{21}}{\mathbf{V}_{11}} \right), \quad (4.60)$$

and is measured positive clockwise from the  $\hat{\mathbf{T}}$  axis to the semimajor axis of the error ellipse. The out-of-plane component of the ellipsoid is associated with the error in time of arrival to the B-plane, denoted by  $\sigma_3$ , and is calculated by dividing the square root of the component of  $\mathbf{P}_B$  associated with  $\hat{\mathbf{S}}$  by  $v_\infty$ .

#### 4.2.4 Validation of Linearity

Inspecting results obtained through Monte Carlo simulations will verify that the linear state model assumption made in the formulation of the Kalman filter algorithm is valid. Using the same long- and short-period comet sample orbits employed in Sec. 2.4, 100 different orbit

solutions are obtained from 91 optical observations spaced one day apart, taken from a single observatory with angular resolution  $\eta = 0.1$  arcseconds, located at the same heliocentric position as the Earth. The observations contain normally distributed random noise with zero mean and standard deviation equal to  $\eta$ . The samples are truncated at  $\pm 2\eta$ . Perturbations due to comet outgassing are not included. Each orbit solution has a covariance matrix  $\mathbf{P}_b$ , resulting in 100 different error ellipses centered on each of the 100 B-plane intersection points, with the distribution of the points themselves mimicking the shape of an ellipse. Each error ellipse is characterized by  $\sigma_1$ ,  $\sigma_2$ ,  $\sigma_3$ , and  $\theta$ . Average values of these parameters should agree fairly well with values determined from a single covariance matrix calculated from the 100 Kalman filter solutions of state deviation at the time of collision. Figs. 7 and 8 show the 100 B-plane intersection points, along with the  $1\sigma$  error ellipse calculated from the single covariance matrix and centered on the mean coordinates of  $B_T$  and  $B_R$  (the  $2\sigma$  and  $3\sigma$  error

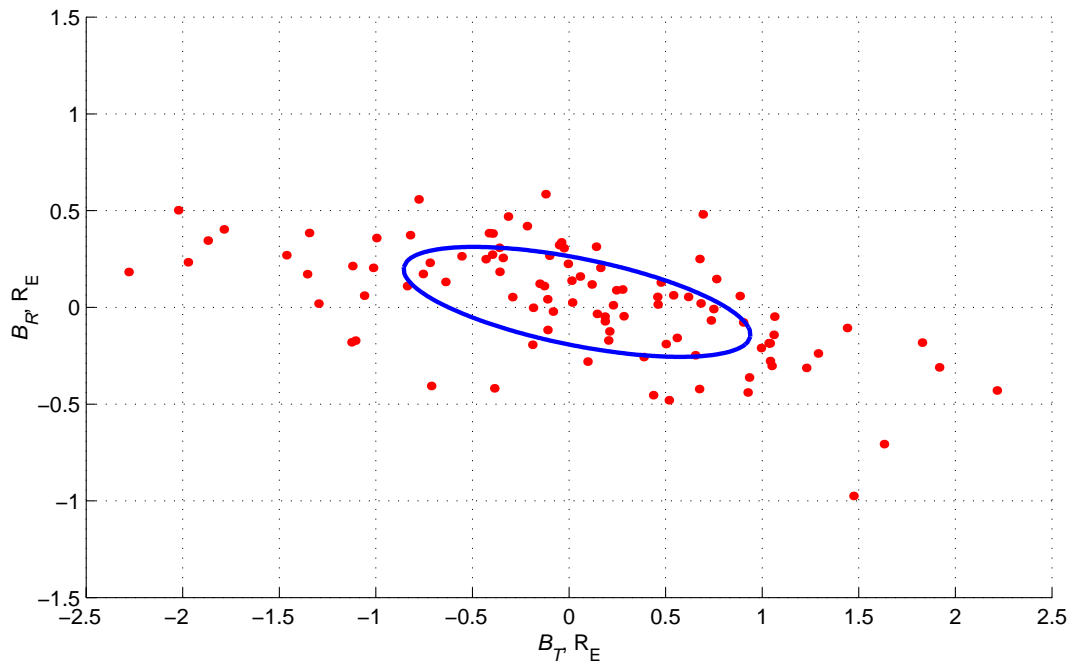


**Figure 7. Error ellipse for a sample long-period comet after 91 observations ( $1\sigma$ )**

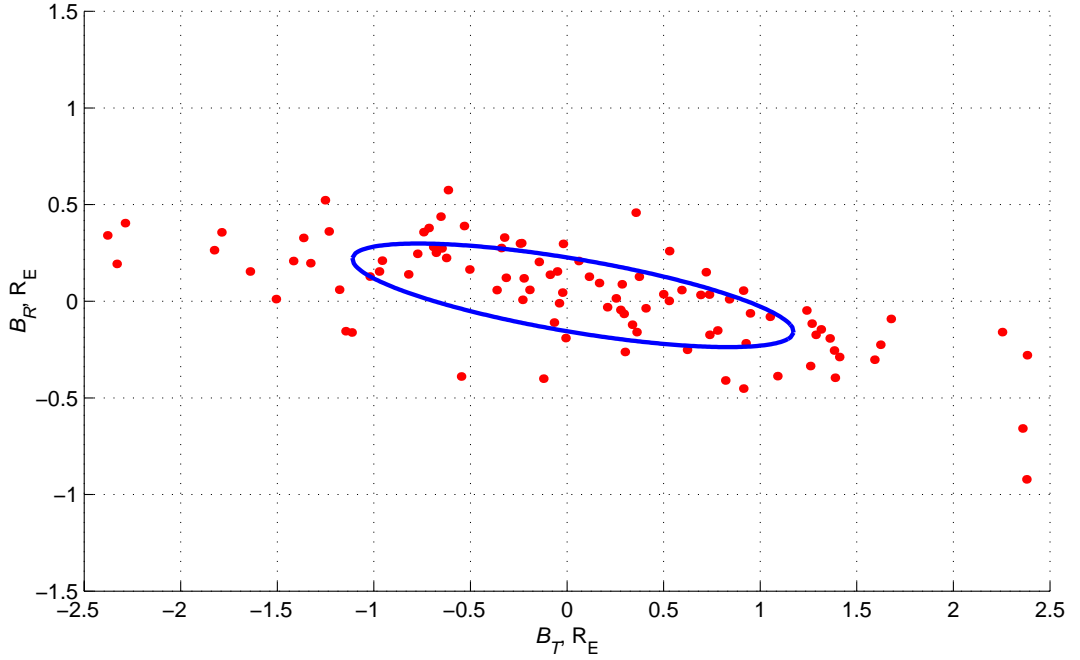


**Figure 8. Error ellipse for a sample short-period comet after 91 observations ( $1\sigma$ )**

ellipses can be calculated by simply multiplying the  $1\sigma$  values by 2 or 3 accordingly). For clarity, the error ellipses associated with each intersection point have been omitted, so Figs. 9 and 10 are supplied to show how the size and orientation of these ellipses are virtually the same for each Monte Carlo simulation, with only slight variations from the mean values, represented in the figures by a blue line. The similarity in the size and orientation of the ellipses is evidence of linearity, as well as the similarity of the average values to the single values of  $\sigma_1$ ,  $\sigma_2$ ,  $\sigma_3$ , and  $\theta$ , listed in Table 1 for comparison. In other words, because the problem is linear, every orbit solution covariance at the designed time of collision will be virtually the same no matter where the B-plane intersection point is located. Since the covariance matrix can be used to describe orbit determination accuracy, the need to run further Monte Carlo cases is eliminated, saving time and computer resources.

Since the perturbation due to outgassing is small, the problem remains linear when

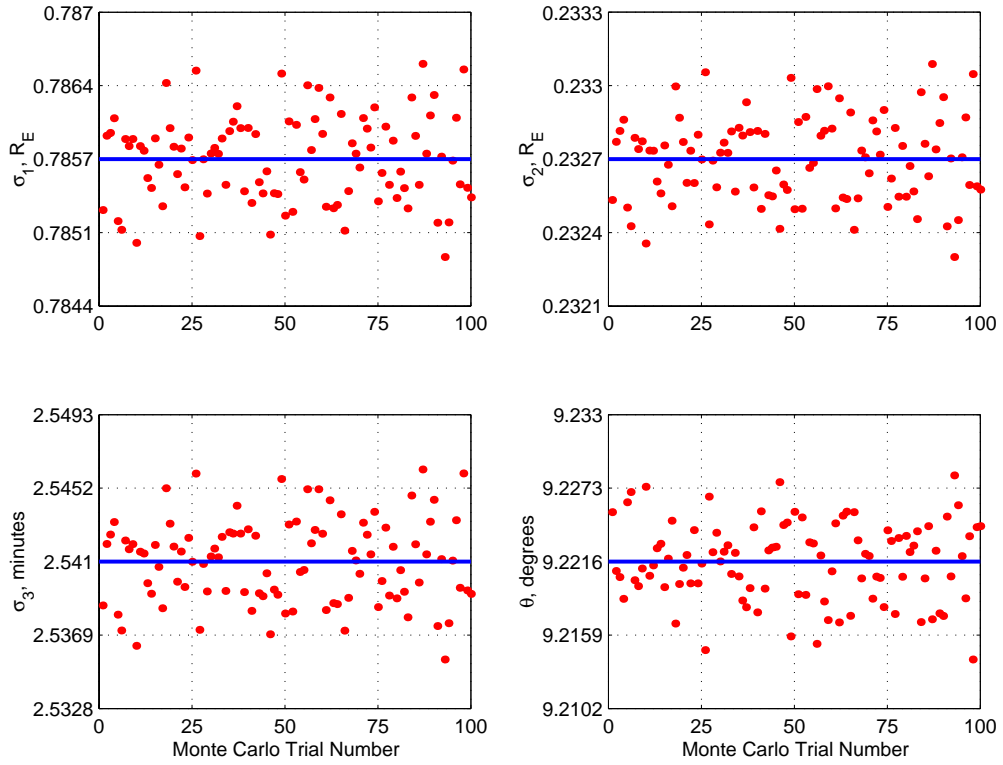


**Figure 9. Variation in error ellipse parameters for a sample long-period comet after 91 observations**

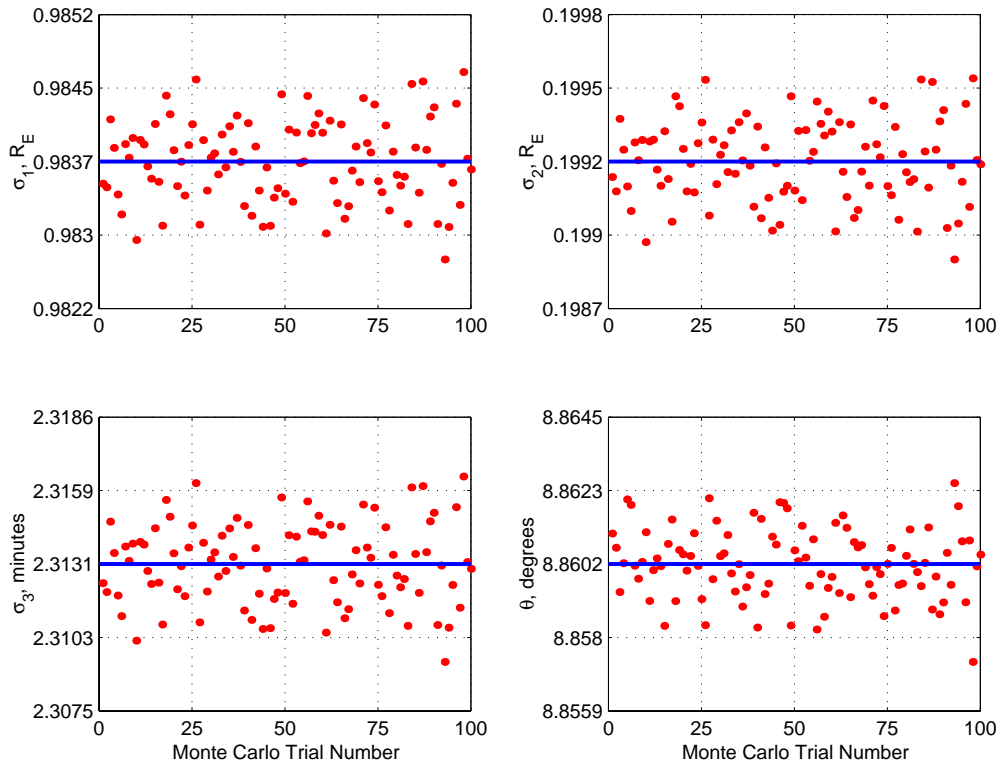


**Figure 10. Variation in error ellipse parameters for a sample short-period comet after 91 observations**

**Table 1. Error Ellipse Parameters for Sample Long- and Short-Period Comets**

	Long-period		Short-period	
	Single	Average	Single	Average
$\sigma_1$ ( $R_E$ )	0.914713	0.785722	1.158412	0.983721
$\sigma_2$ ( $R_E$ )	0.224407	0.232689	0.188408	0.199222
$\sigma_3$ (minutes)	2.491799	2.541044	2.439856	2.313072
$\theta$ (degrees)	11.334516	9.221617	9.591973	8.860158
$B_T$		0.041637		0.030882
$B_R$		0.028503		0.030710

**Table 2. Error Ellipse Parameters for Sample Long- and Short-Period Comets with Outgassing Included**

	Long-period		Short-period	
	Single	Average	Single	Average
$\sigma_1$ ( $R_E$ )	0.923522	0.796227	1.166215	0.992968
$\sigma_2$ ( $R_E$ )	0.229514	0.236704	0.193971	0.204095
$\sigma_3$ (minutes)	2.537502	2.585841	2.490257	2.366148
$\theta$ (degrees)	10.903420	8.676846	9.329242	8.504838
$B_T$		-0.068534		-0.084936
$B_R$		0.014652		0.016525

these perturbations are included. Table 2 lists values of the error ellipse parameters for the outgassing case. By comparing the values in Table 2 with the values in Table 1, the effect of comet outgassing is an increase in the size of the  $1\sigma$  error ellipse, signaling slightly less accurate orbit determination.

#### 4.2.5 Collision Probability

With the proof presented in the previous section that the linearity assumption is valid, Monte Carlo simulations are no longer required. The nominal comet trajectory is used as the reference trajectory in the Kalman filter orbit determination sequence, and as such, passes through the center of the Earth. Under this formulation the metric for describing how well the orbit has been determined is not an actual miss distance, but rather an Earth-collision

probability. The projection of the Earth onto the B-plane is a disk, and the probability of impact can be computed by integrating the bivariate Gaussian probability density function,

$$f_{TR} = \frac{1}{2\pi\sigma_T\sigma_R\sqrt{1-\rho_{TR}^2}} \exp \left\{ -\frac{\left(\frac{B_T}{\sigma_T}\right)^2 - 2\rho_{TR}\left(\frac{B_T}{\sigma_T}\right)\left(\frac{B_R}{\sigma_R}\right) + \left(\frac{B_R}{\sigma_R}\right)^2}{2(1-\rho_{TR}^2)} \right\}, \quad (4.61)$$

over the effective cross-sectional area of the Earth, which accounts for the gravity of the planet that was neglected in the construction of the B-plane. The effective collision radius is given by Eq. (8.3-30) in Ref. [5] as

$$\bar{R}_E = \frac{R_E}{v_\infty} \sqrt{v_\infty^2 + \frac{2\mu_E}{R_E}}, \quad (4.62)$$

where  $R_E$  is the physical radius of the Earth and  $\mu_E$  is the gravitational parameter of the Earth. The variables  $\sigma_T$  and  $\sigma_R$  in Eq. (4.61) are the standard deviations in  $B_T$  and  $B_R$  and are related to  $\sigma_1$  and  $\sigma_2$  through the expressions

$$\sigma_T = \sqrt{(\sigma_1 \cos \theta)^2 + (\sigma_2 \sin \theta)^2}, \quad (4.63)$$

$$\sigma_R = \sqrt{(\sigma_1 \sin \theta)^2 + (\sigma_2 \cos \theta)^2}. \quad (4.64)$$

The variable  $\rho_{TR}$  is the correlation coefficient of  $\sigma_T$  and  $\sigma_R$ .

Numerical integration of Eq. (4.61) is performed by constructing a coarse grid on the B-plane. At each coarse grid point, Eq. (4.61) is evaluated at every point on a fine grid that approximates a circle of radius  $\bar{R}_E$ , and is multiplied by the area of the fine grid square. The probability that the comet passes through the B-plane somewhere inside this circle is simply

the sum of these products. Contours of constant  $f_{TR}$  are ovals, as in Fig. 11, which shows contours of constant collision probability for the long-period comet sample case without outgassing. The maximum value of collision probability occurs at the origin, and the figure can be interpreted as follows: if the calculated orbit crosses the B-plane at the origin (signifying a predicted collision at the center of the Earth), the probability of collision is 0.796; if the calculated orbit crosses the B- plane at (2,0) where it intersects the contour labeled  $-1$ , the probability of collision is 0.1; points outside the contour labeled  $-6$  signify less than a one- in-a-million chance that a collision will occur. Therefore for this sample case, with 91 optical observations taken from a single observatory once per day, the confidence in predicting an Earth collision can never be greater than 0.796, or 79.6%. When perturbations due to comet outgassing are included, this probability decreases to 78.9%.

Fig. 12 shows maximum collision probability, denoted by  $\kappa_0$ , as a function of tracking duration from a single observatory for both the long- and short-period sample

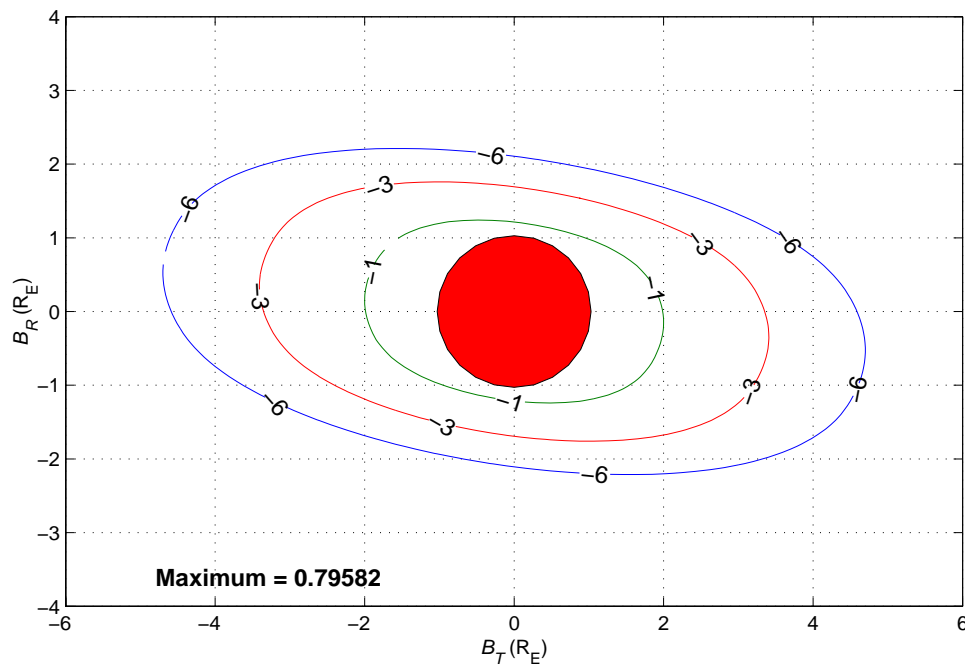
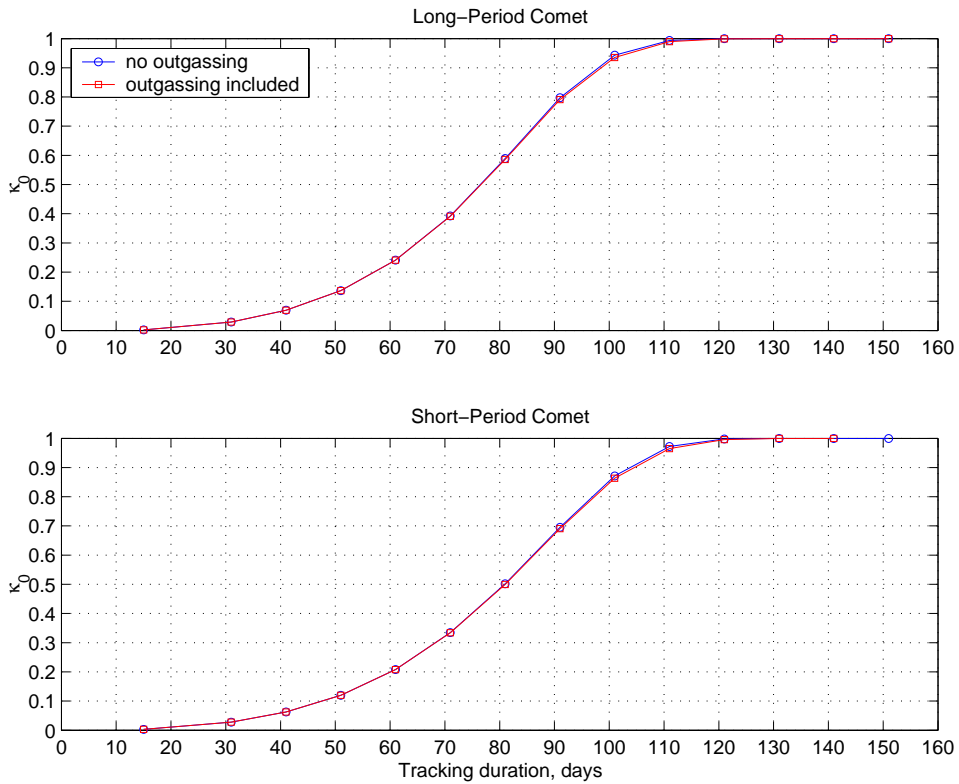


Figure 11. Earth collision probability for a sample long-period comet after 91 observations



**Figure 12. Maximum collision probability as a function of tracking duration for sample long- and short-period comets**

comets, with and without perturbations due to outgassing included. This figure clearly shows the collision probability results obtained from 15 to 100 days of observations, where  $\kappa_0$  reaches approximately 0.9. However, the results of interest are at longer tracking durations where the curves appear to level off and the collision probability is 0.99 or above. It is also difficult to distinguish any significant effect outgassing has on the results. Plotting  $1 - \kappa_0$  versus tracking duration on a logarithmic scale, as in Fig. 13, makes the results much easier to interpret. It is clear from this figure that outgassing does indeed introduce uncertainty in the orbit solution. Fig. 14 shows the B-plane collision probability for the 141-day tracking interval. Comparing with Fig. 11, the ovals are now smaller in size, and the collision probability at the point (2,0) is now less than  $10^{-6}$ .

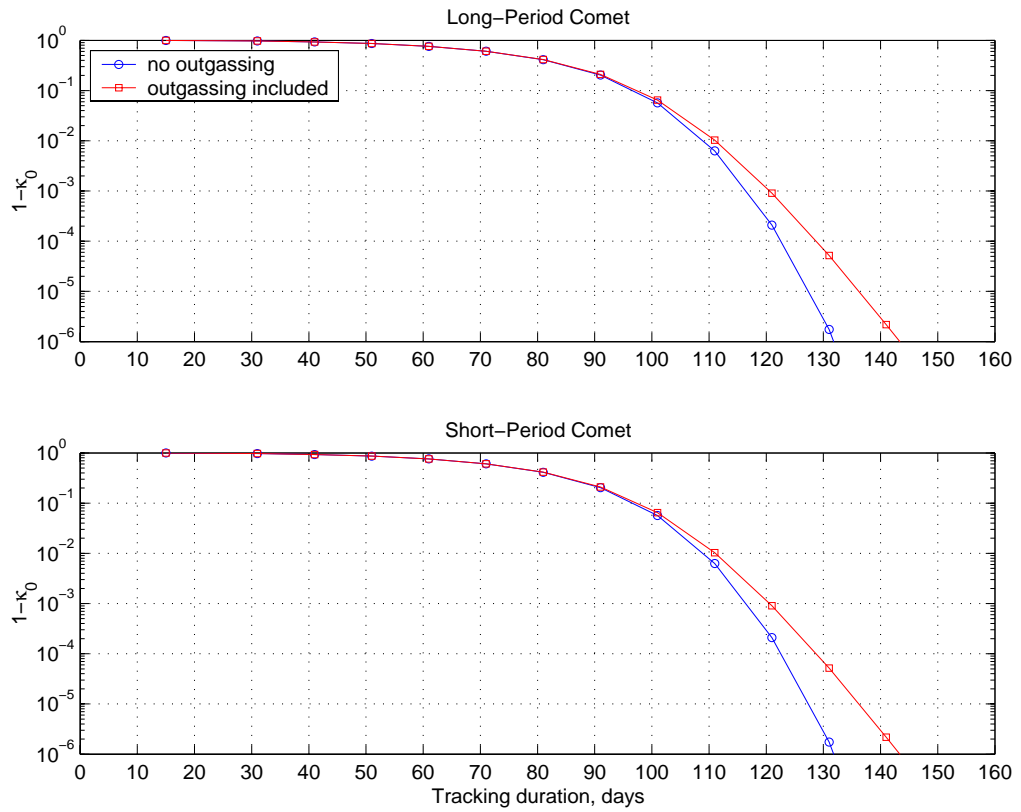


Figure 13. Maximum collision probability as a function of tracking duration on a logarithmic scale for sample long- and short-period comets

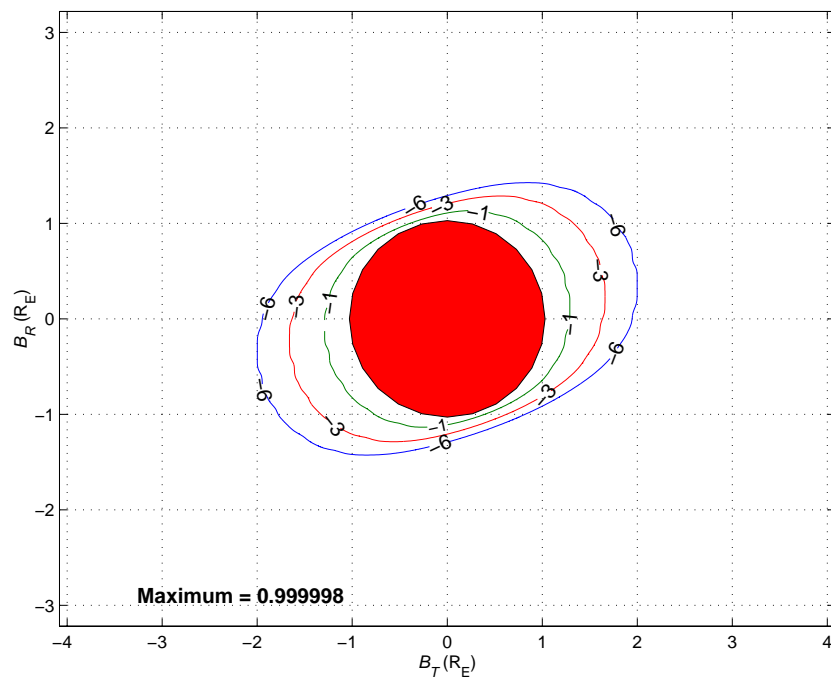


Figure 14. Earth collision probability for a sample long-period comet after 141 observations

## 5 Observatory Location and Observation Schedule

The results for the sample cases of the long- and short-period comets have been used thus far to aid in the presentation of the concepts and the method used to describe how well an Earth-impacting comet orbit can be determined. B-plane error ellipses and collision probabilities have been compared for these two cases, but general conclusions about the best observatory location or tracking schedule cannot be made based on these two cases alone. Therefore, a family of comets on Earth-impacting trajectories is created with varying inclinations to serve as a representative set of the real-life population of possible impactors, and orbit determination accuracies are analyzed for this family of comets. The orbits are determined from angular measurements over several different tracking intervals, and from single or multiple space-based observatories in circular orbits around the Sun at varying heliocentric distances. Radar measurements of range are also included in some cases. The results of this analysis will make it possible to compare various telescope configurations and observation schedules to be used for determining the orbits of Earth-impacting comets.

The family of comets on which the remainder of the analysis will be focused contains five orbits with inclinations of  $5^\circ$ ,  $45^\circ$ ,  $90^\circ$ ,  $135^\circ$ , and  $175^\circ$ , chosen to characterize low and high inclination orbits and direct and retrograde motion. Inclinations of  $0^\circ$  and  $180^\circ$  are not included because these cases will cause all of the elements in the first, fourth, and fifth columns of the  $6 \times 6$  matrix on the left hand side of Eq. (4.9) to be zero, and finding a preliminary orbit solution will not be possible. Based on the results of the sample comets in the previous section, increasing the orbital period (or increasing the aphelion distance from say, 40 to 300 AU) does not cause a significant change in collision probability, therefore all orbits in this representative set have an aphelion distance of 300 AU and a perihelion

distance of 0.1 AU. The comet orbits also have  $\Omega$ ,  $\omega$ , and  $v_0$  in common, with values of  $30^\circ$ ,  $143.6^\circ$ , and  $-164.8^\circ$ , respectively.

## 5.1 Single Observatory at Earth

The most convenient location for an observatory would be on the Earth, or in low Earth orbit. In orbit determination simulations performed for this study, it is assumed that the observatory is located at the center of the Earth because the distance between the observatory and the comet during the tracking interval is so large (approximately 5 AU). All observations are assumed possible; situations where the Sun or other bodies would interfere with observing the comet are ignored.

Fig. 15 contains plots of collision probability,  $\kappa$ , as a function of tracking interval for a single observatory coincident with the Earth. The probability was calculated at three

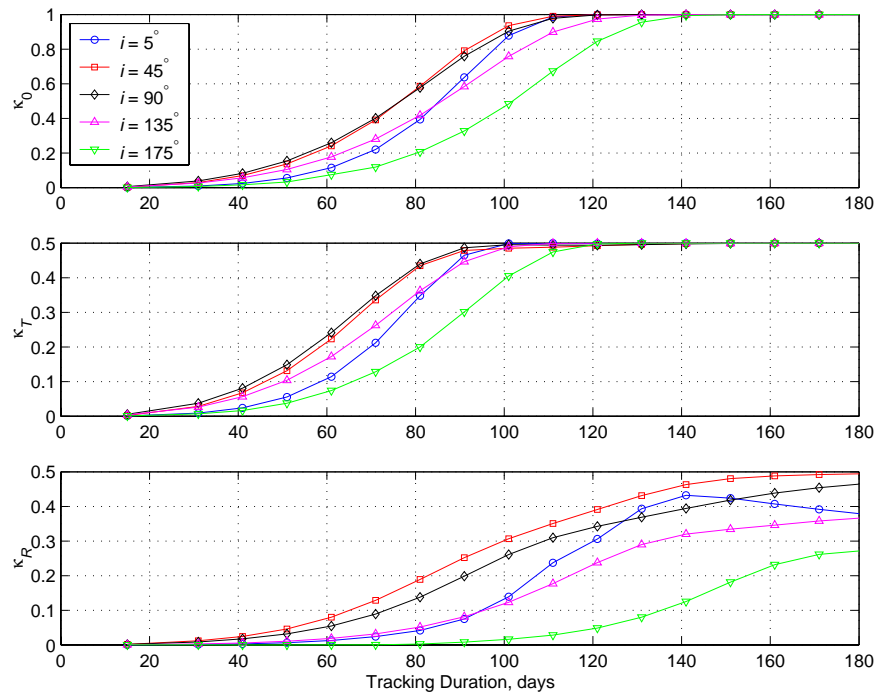
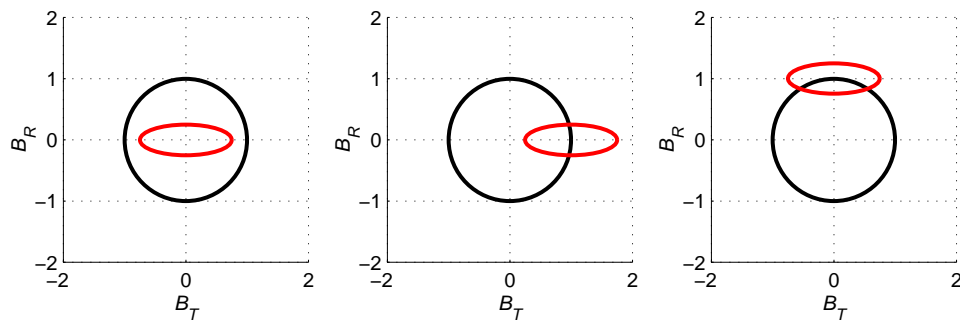


Figure 15. Collision probability results from a single Earth observatory

selected points in the B-plane for each of the comets in the test set: at the center of the Earth, and at the surface of the Earth in both the  $B_T$  and  $B_R$  directions. Collision probability at the center of the Earth is denoted by  $\kappa_0$ , and at the surface of the Earth along the  $B_T$  and  $B_R$  axes, collision probability is denoted by  $\kappa_T$  and  $\kappa_R$ , respectively. One obvious characteristic of the curves in Fig. 15 is that each approaches a maximum value of  $\kappa$  at long tracking durations. This behavior is explained by visualizing collision probability as the area of an ellipse contained inside a disk. In the limit, this area approaches 1 if the ellipse center is located at the center of the disk, as shown in the plot on the left of Fig. 16. The area of the same ellipse with its center located at the surface of the disk approaches 0.5, as shown in the middle plot (half of the ellipse lies inside the Earth disk, and half lies outside). However, if the same ellipse is located at some other point on the surface of the disk as shown in the plot on the right, the area inside could be less than 0.5, depending on the size and orientation of the ellipse. In the limit the ellipse would become sufficiently small so that the area inside would approach 0.5, no matter where on the surface of the disk it was located. Referring back to Fig. 15,  $\kappa_0$  approaches the limit at 1, and  $\kappa_T$  approaches the limit at 0.5. The limit is approached much more slowly for  $\kappa_R$  due to the orientation of the error ellipse. It is difficult to discern the variation in  $\kappa$  at these limits, so the behavior is shown in detail by plotting



**Figure 16. Collision probability for central and limb impacts**

$1-\kappa_0$ ,  $0.5-\kappa_T$ , or  $0.5-\kappa_R$  on a logarithmic scale, as in Fig. 17. If collision probabilities of 0.99 are of interest, then approximately 111 observations from a single telescope at 1 AU are needed to accurately determine the direct comet orbits in the test set. For the retrograde orbits, 130 to 140 observations are needed to achieve the same level of accuracy. This difficulty is due to poor orbit geometry between the observatory and the comet. Fig. 18 shows the heliocentric orbits of the comet (red) and the observatory (blue) over a 121-day tracking interval for the direct comet orbit with  $i = 5^\circ$  and the retrograde comet with  $i = 175^\circ$ . The geometry for the direct comet case results in larger heliocentric parallax between the observatory and the Sun-comet line than for the retrograde comet case. This larger parallax is beneficial to orbit determination accuracy because it helps determine the distance between

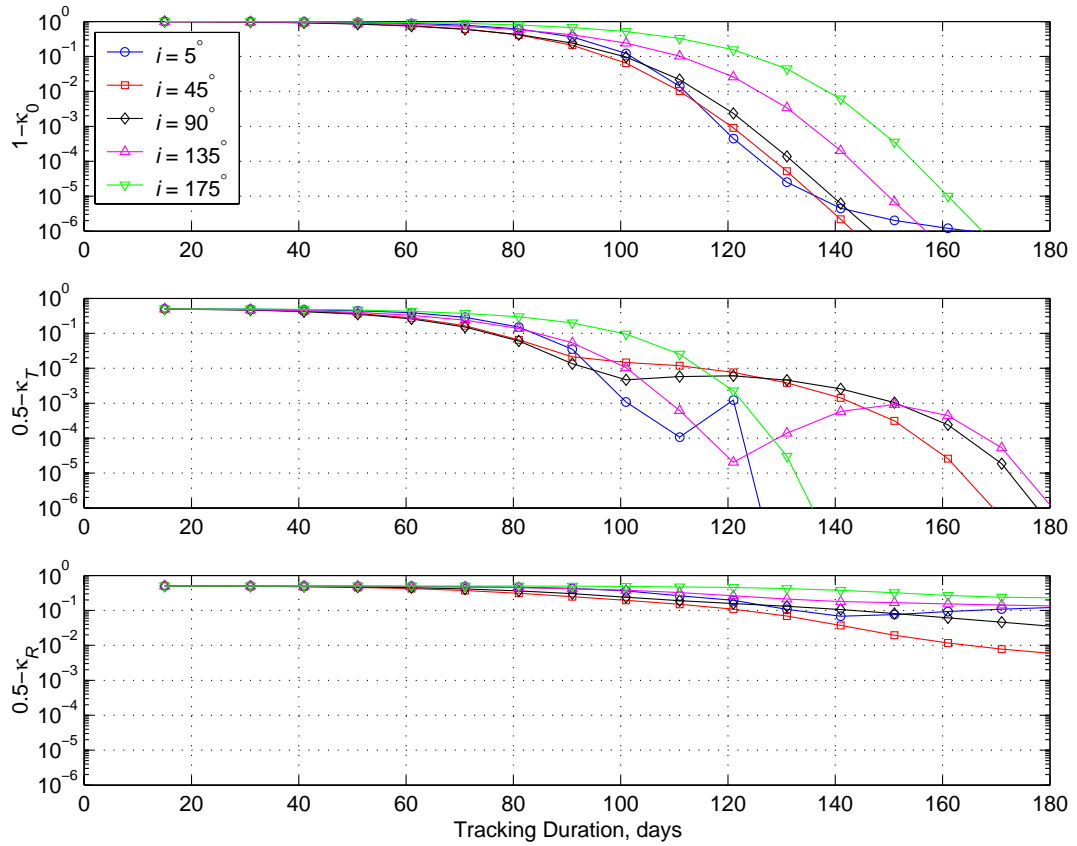


**Figure 17. Collision probability results from a single Earth observatory on a logarithmic scale**

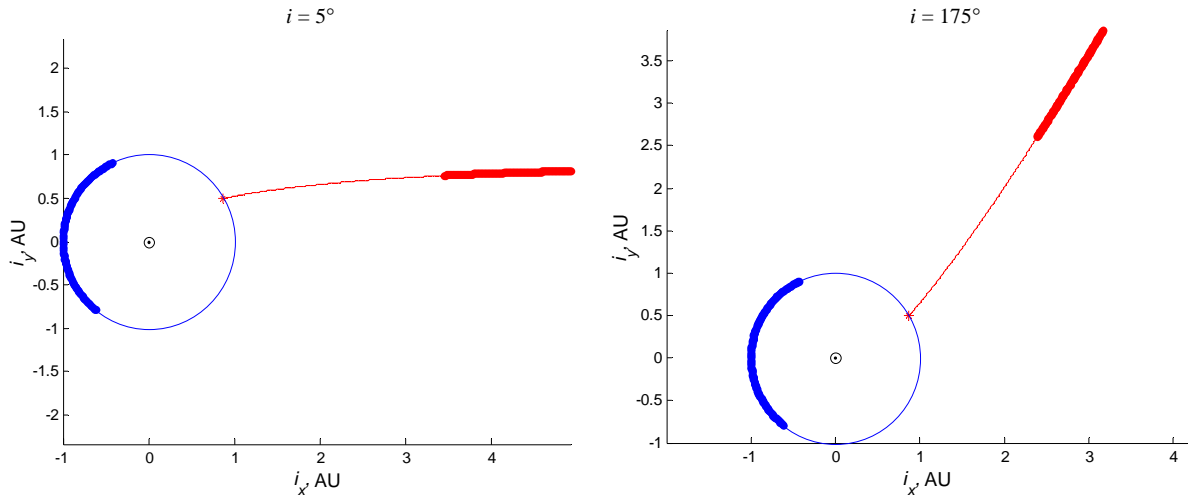


**Figure 18. Orbit geometry between an observatory at 1 AU and direct and retrograde comets**

the comet and the observatory along the line of sight. The subject of parallax will be discussed in more detail in the next section.

As previously explained,  $\kappa_T$  and  $\kappa_R$  are sensitive to the orientation of the error ellipse. As the tracking duration lengthens, the orientation of the error ellipse changes so that the angle between the semimajor axis and the direction of the heliocentric velocity of the comet increases. This change in orientation is the reason why the  $\kappa_T$  curves in Fig. 17 have a “bump”. With a small number of observations, the majority of the orbit determination error is along track (in a direction parallel to the heliocentric velocity of the comet). As more observations are collected the error in this direction decreases, and the orientation of the error ellipse changes. Fig. 19 shows this behavior. On the top is the error ellipse for the 45° inclination comet after 61 observations, and on the bottom is the error ellipse for the same comet after 121 observations. Also shown is the direction of the heliocentric velocity of the comet projected into the B-plane, represented by the green lines. The error ellipse on the top is much larger and the semimajor axis is oriented along the direction of the velocity of the comet, signaling that the majority of the error is along track. On the bottom, the error ellipse

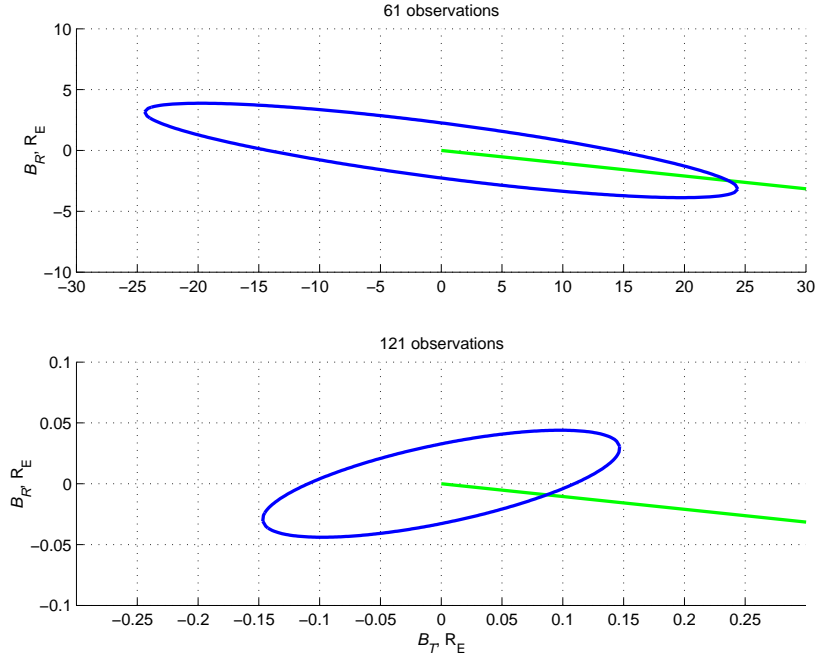


**Figure 19. Orientation of error ellipses for a long-period comet with 45° inclination**

is smaller, and the angle between the semimajor axis and the velocity is larger, evidence that as the tracking duration increases the importance of the error along track decreases.

## 5.2 Single Observatory in a Circular Orbit at 1 AU

Although an observatory located at the center of the Earth approximates a convenient location, such as low Earth orbit, there may be other positions along the heliocentric orbit of the Earth that result in better orbit determination accuracy. One way to investigate this is to examine the size of the error ellipse resulting from observatory locations that vary in increments of 5° around the heliocentric orbit of the Earth. Tracking durations of five days are used to determine the orbit solution and the associated error ellipse for each 5° increment. The results are presented in Fig. 20, which shows the semimajor axis of the error ellipse,  $\sigma_1$ , versus the angle,  $\gamma$ , in the ecliptic plane between the observatory and comet position vectors

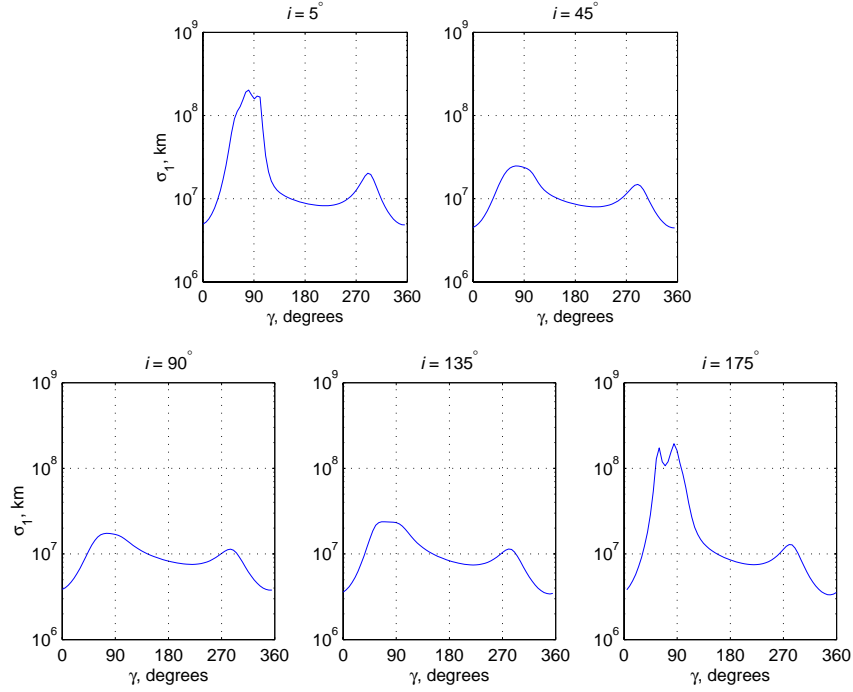


**Figure 20. Semimajor axis of error ellipse after 5 observations as a function of the angle between the observatory and the Sun-comet line**

at the time of the first observation. Smaller values of  $\sigma_1$  represent orbit solutions with less uncertainty than those with larger values of  $\sigma_1$ . There is similarity in the variation of  $\sigma_1$  between the  $i = 5^\circ$  and  $i = 175^\circ$  cases, and also between the  $i = 45^\circ$  and  $i = 135^\circ$  cases. Also, the comet with  $i = 90^\circ$  has the least amount of variation in  $\sigma_1$  due to the fact that the orbit plane is perpendicular to the ecliptic plane, and the comet appears to be directly overhead from the point of view of the observatory. Minimum values of  $\sigma_1$  occur when  $\gamma$  is approximately  $0^\circ$  (or  $360^\circ$ ), with a secondary minimum near  $\gamma = 180^\circ$ ; peaks in  $\sigma_1$  occur when  $\gamma$  is near  $90^\circ$  or  $270^\circ$ . These variations in  $\sigma_1$  are due to the time rate of change of heliocentric parallax,  $d\beta/dt$ , given by

$$\frac{d\beta}{dt} = \frac{\|\mathbf{r}_\infty \times \mathbf{v}_\infty\|}{\|\mathbf{r}_\infty\|^2}. \quad (5.1)$$

Minimum values of  $\sigma_1$  occur at maximum values of  $d\beta/dt$ , where  $\gamma$  is near  $0^\circ$  or  $180^\circ$ , as shown in Fig. 21. Points of minimum and maximum  $d\beta/dt$  are labeled with the corresponding value of  $\gamma$ . At the points of maximum parallax rate, the observatory is moving in a direction perpendicular to the Sun-comet line. The maximum values of  $d\beta/dt$  indicate that these locations produce the most apparent motion between the observatory and the comet. Because the distance between the observatory and the comet is so large during the tracking interval, the comet appears to be stationary. Therefore, the main contributor to the change in parallax is the motion of the observatory.

The results presented in Fig. 21 are confirmed by studying parallax rate through an analytical approach, where the comet is placed on the  $\hat{i}_x$  axis at a distance of 5 AU and

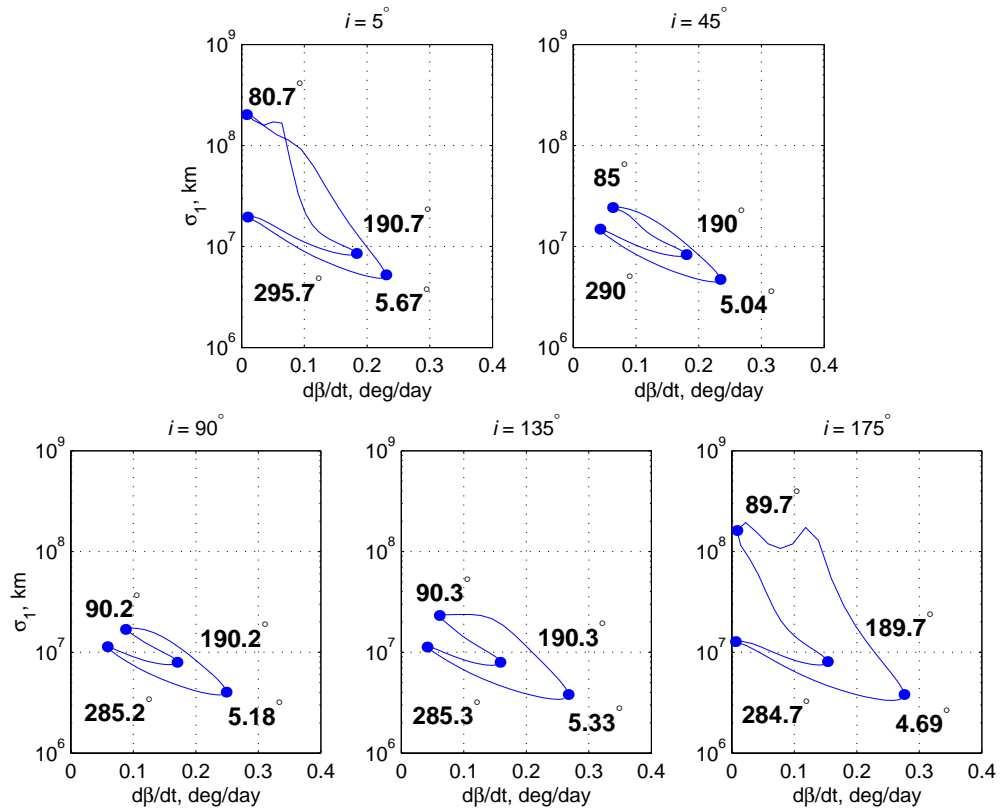
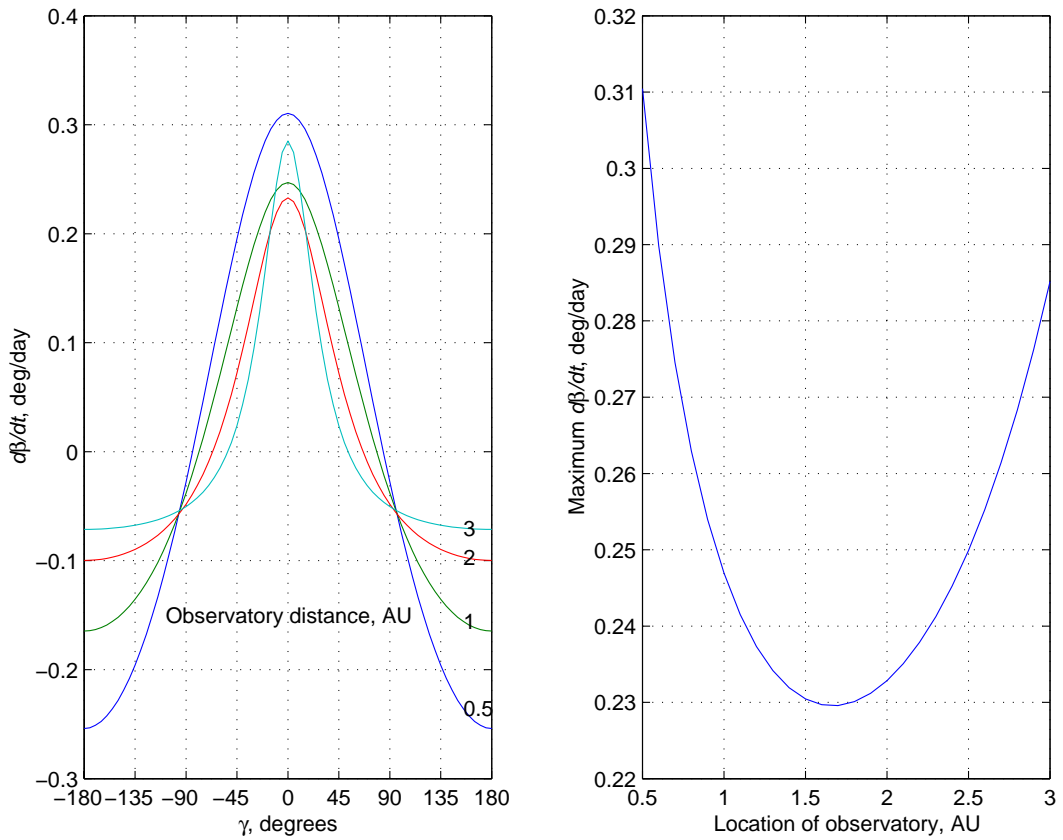


Figure 21. Semimajor axis of error ellipse after 5 observations as a function of time rate of change of parallax

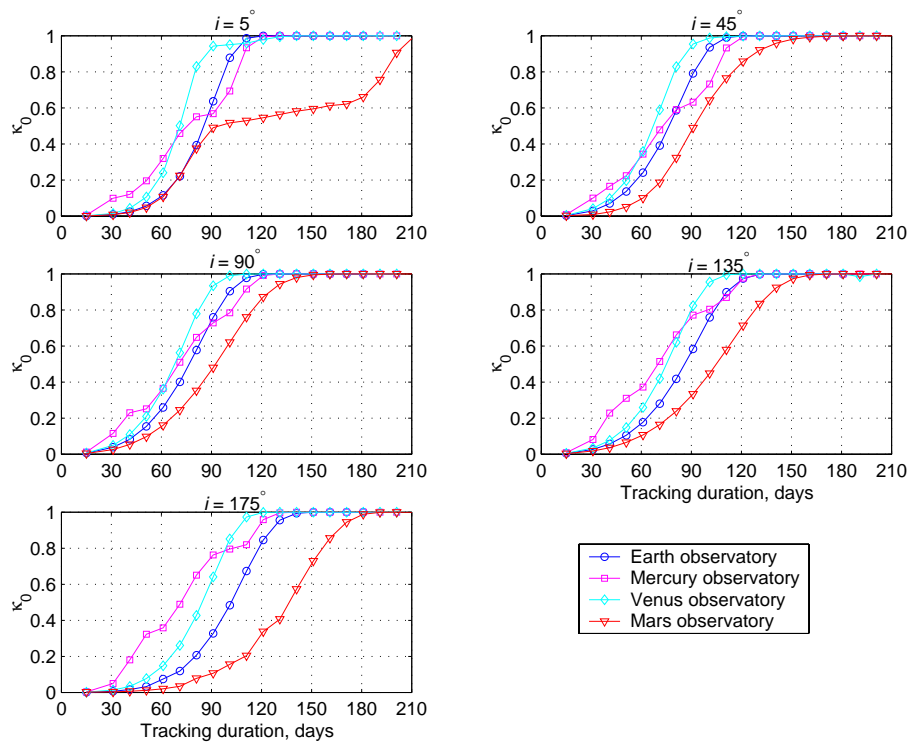
$d\beta/dt$  is calculated at  $5^\circ$  increments around circular, heliocentric observatory orbits of various radii. The plot on the left of Fig. 22 shows the relationship between  $d\beta/dt$  and  $\gamma$  for these hypothetical cases. Maximum  $|d\beta/dt|$  occurs when  $\gamma=0^\circ$ , with a secondary maximum when  $\gamma=180^\circ$ ; minimum  $|d\beta/dt|$  occurs when  $\gamma$  is between  $\pm 45^\circ$  and  $\pm 90^\circ$ . In particular, the curve corresponding to an observatory radius of 1 AU is at maximum  $|d\beta/dt|$  when  $\gamma=0^\circ$  or  $180^\circ$ , and minimum  $|d\beta/dt|$  when  $\gamma$  is approximately  $80^\circ$  or  $280^\circ$ . These results agree well with those presented in Fig. 21. Moving the observatory orbit inside 1 AU to 0.5 AU, or outside 1 AU to 3 AU, increases the maximum parallax rate, as shown in the plot on



**Figure 22. Time rate of change of parallax as a function of observatory orbit radius for a hypothetical comet with  $i = 0^\circ$**

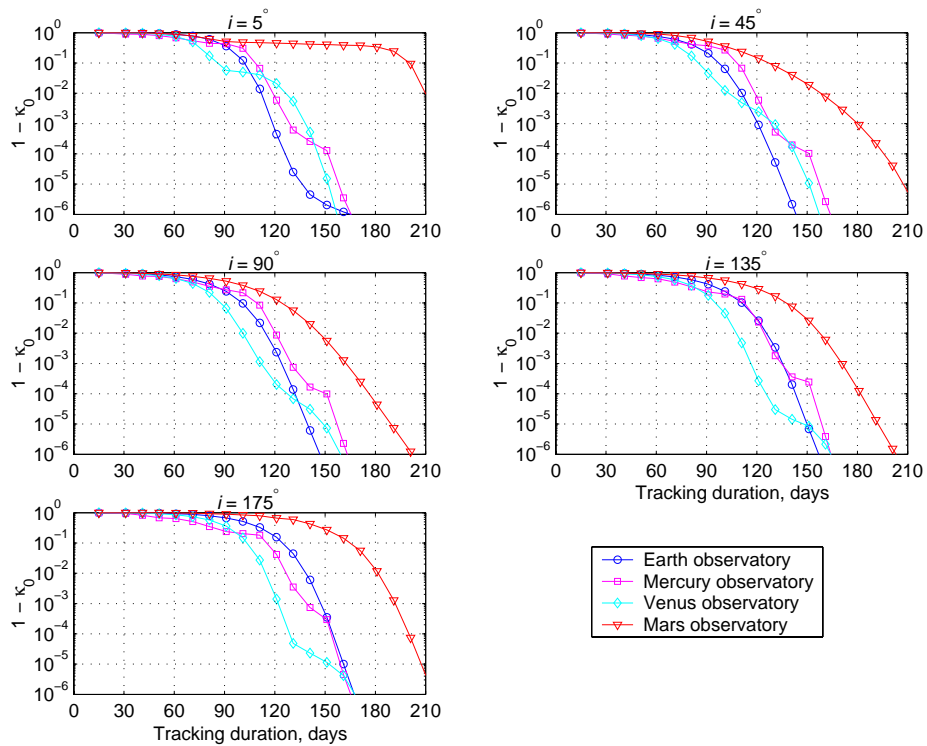
the right of Fig. 22. Since better orbit determination is obtained when  $d\beta/dt$  is maximum, the best locations for an observatory are in an orbit with a small radius, where the observatory would be traveling very fast around the Sun, or in a larger orbit closer to the comet. However, the cost of delivering an observatory to such orbits may not be justifiable based on the small increases in  $d\beta/dt$  shown in Fig. 22. An observatory at 1 AU could perform just as well if the tracking duration was sufficiently long, if additional observatories were available to collect observations, or if the observations also included measurements of range.

Fig. 23 shows maximum collision probability,  $\kappa_0$ , versus tracking duration for four different observatory orbits, corresponding to Mercury, Venus, Earth, and Mars orbit radii. The results for short tracking intervals, when the main factor in orbit determination accuracy



**Figure 23. Collision probability as a function of tracking duration for Mercury, Venus, Earth, and Mars observatories**

is parallax rate, agree with the conclusions drawn in the previous discussion. In each case the Mercury and Venus observatories out perform the Earth observatory, and the Earth observatory out performs the Mars observatory. However, as the tracking duration increases the orbit determination accuracy is improved by the additional observations, and the Earth observatory performs just as well, or better, than the others for direct comet orbits, as shown in Fig. 24. For retrograde comet orbits the comet is moving in a direction opposite to that of the observatory, making the parallax rate larger, and the Mercury and Venus observatories still produce the best orbit determination for a majority of the tracking interval for these cases. However, after approximately 170 days the Earth observatory results in the same orbit determination accuracy as the Mercury and Venus observatories. In all cases the Mars observatory produces the worst orbit determination accuracy, which is consistent with the hypothetical results presented previously. The orbit radius of Mars is near the minimum of



**Figure 24. Collision probability as a function of tracking duration for Mercury, Venus, Earth, and Mars observatories on a logarithmic scale**

the curve on the right of Fig. 22. Since the Earth observatory can be made to achieve the same orbit determination accuracy as observatories with higher parallax rates, there is no need to expend the additional cost of transferring an observatory to an orbit outside a heliocentric radius of 1 AU.

### 5.3 Multiple Observatories in Circular Orbits at 1 AU

The direction from which the comets are traveling on their Earth-impacting trajectories will not be known ahead of time, and it may even be necessary to track several targets at the same time. It is impossible to ensure that a single observatory could be placed in a location that allows maximum time rate of change of parallax between it and a comet. However, the odds of achieving the desired geometry are increased by adding a second or third observatory in the same heliocentric orbit. Using a multi-observatory configuration results in simultaneous angular measurements, which is equivalent to measurements with large parallax and no time lapse. Also, the number of available observations can be doubled or tripled, which will also improve orbit determination accuracy. Several different observatory configurations are investigated, with observatories placed at the Sun-Earth Lagrange points  $L_3$ ,  $L_4$ , or  $L_5$  shown

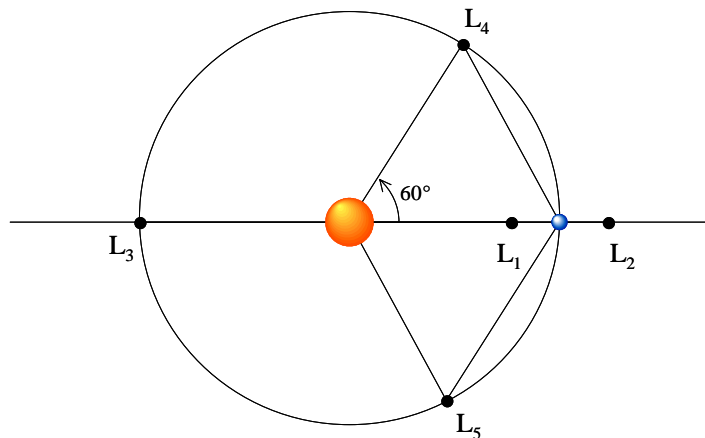


Figure 25. Location of Sun-Earth Lagrange points

in Fig. 25. The  $L_3$  Lagrange point is  $180^\circ$  ahead of the Earth, the  $L_4$  point is  $60^\circ$  ahead of the Earth, and the  $L_5$  point is  $60^\circ$  behind the Earth.

Fig. 26 shows maximum collision probability versus tracking duration on a logarithmic scale for various observatory configurations. The curves corresponding to the single Earth observatory are the same curves shown in Figs. 23 and 24. There are three curves corresponding to systems consisting of two observatories, each with one observatory located at the center of the Earth, and the second at a Sun-Earth Lagrange point. A curve is shown corresponding to a configuration with three observatories, one at the center of the Earth and one each at the Lagrange points  $L_4$  and  $L_5$ . Also shown is a single observatory located at the center of the Earth that is capable of collecting range measurements good to 1000 km, as well as optical measurements. The single Earth observatory gives the poorest

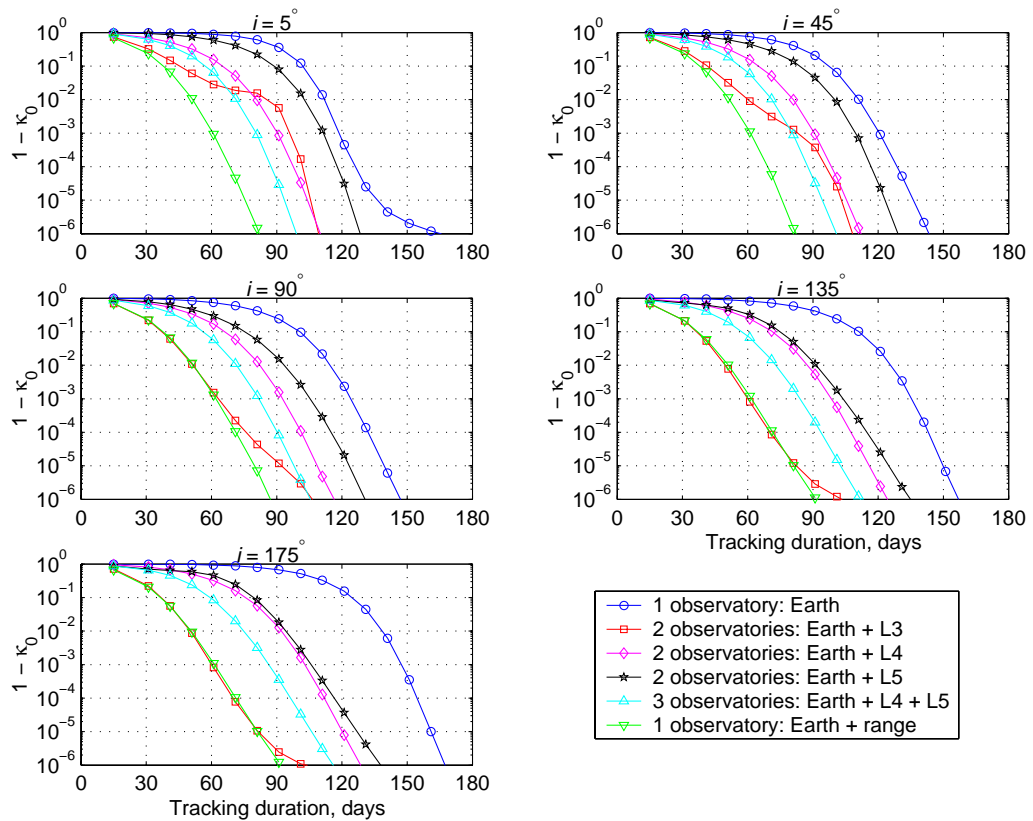


Figure 26. Collision probability results from observatories in circular heliocentric orbits at 1 AU

orbit determination in terms of the time required to achieve a specified value of collision probability. In the direct comet orbit cases, the Earth + L<sub>4</sub> configuration performs better than the Earth + L<sub>5</sub> configuration. The initial orbit geometry is such that the second observatory at L<sub>4</sub> is moving across the Sun-comet line, which increases the time rate of change of parallax. An observatory at L<sub>5</sub> is moving in the same general direction as the comet and does not contribute the same beneficial increase in parallax rate. In the retrograde comet orbit cases, the Earth + L<sub>4</sub> and the Earth + L<sub>5</sub> configurations exhibit similar performance because both systems are moving in the same general direction as the comet, except during longer tracking durations when the L<sub>4</sub> observatory is moving in a direction perpendicular to the Sun-comet line. The system of three observatories, Earth + L<sub>4</sub> + L<sub>5</sub>, is better than both the Earth + L<sub>4</sub> and Earth + L<sub>5</sub> systems, but the best configurations are the two observatory system of Earth + L<sub>3</sub>, and the single Earth observatory capable of range measurements. These systems yield very similar results for retrograde comet orbits because in these cases the orbit geometry is ideal. The line joining the Earth + L<sub>3</sub> observatories is perpendicular to the Sun-comet line, and the parallax between the observatories and the comet is maximum. This configuration is just as effective as a single observatory with range measurement capability, and orbit solutions with very high collision probability will be determined within three months of tracking. For direct comet orbits, the Earth + L<sub>3</sub> observatory geometry is less than ideal. In fact, a tracking duration of approximately 71 days results in zero parallax. Without the parallax benefit, the Earth + L<sub>3</sub> configuration produces less accurately determined orbits than the range observatory. Based on these results, the single Earth observatory with range capability is the best choice for observing all the comets in the test set, producing orbit solutions with maximum collision probability of 0.99 with 51 days of tracking.

As mentioned earlier, with short tracking arcs of angular measurements, the major error at the time of impact is along the comet velocity, i.e. along track. This error results from the fact that the range to the comet is poorly determined by angular measurements. The advantage of range data is to immediately resolve this uncertainty. An approximate relation between range accuracy derived from angular data can be developed based on Fig. 27. Consider two observatories in the same heliocentric orbit that measure the angle  $\gamma$  to locate the comet assuming the comet is along the normal to the line between the observatories. The heliocentric distance to the comet is easily derived from the distance  $D$ , which is given by

$$D = d \tan \gamma. \quad (5.2)$$

Assuming both observatories have an error in  $\gamma$  of  $\eta_\gamma$ , the error in the inferred distance  $D$  is

$$\begin{aligned} \eta_D &= \eta_\gamma d \sec^2 \gamma \\ &= \eta_\gamma d \left[ 1 + \left( \frac{D}{d} \right)^2 \right]. \end{aligned} \quad (5.3)$$

This relationship is plotted in Fig. 28 for  $\eta_\gamma = 0.1$  arcsec. If the two observatories were at the Earth and L<sub>3</sub> ( $d = 1$  AU) the range to a comet at 5 AU can be determined to about 10,000 km. So independent range measurements with measurement accuracy much less than 10,000 km

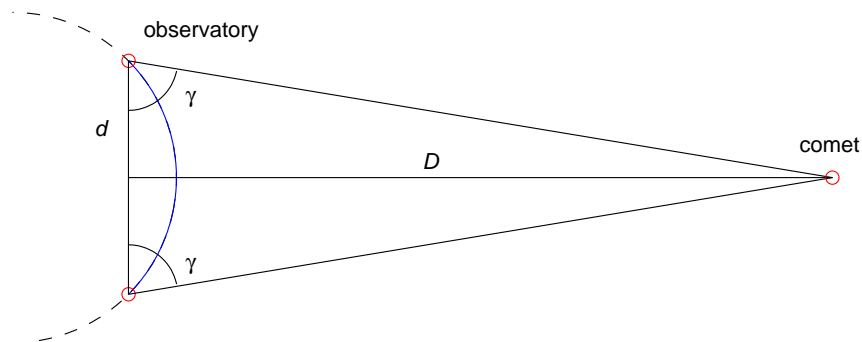
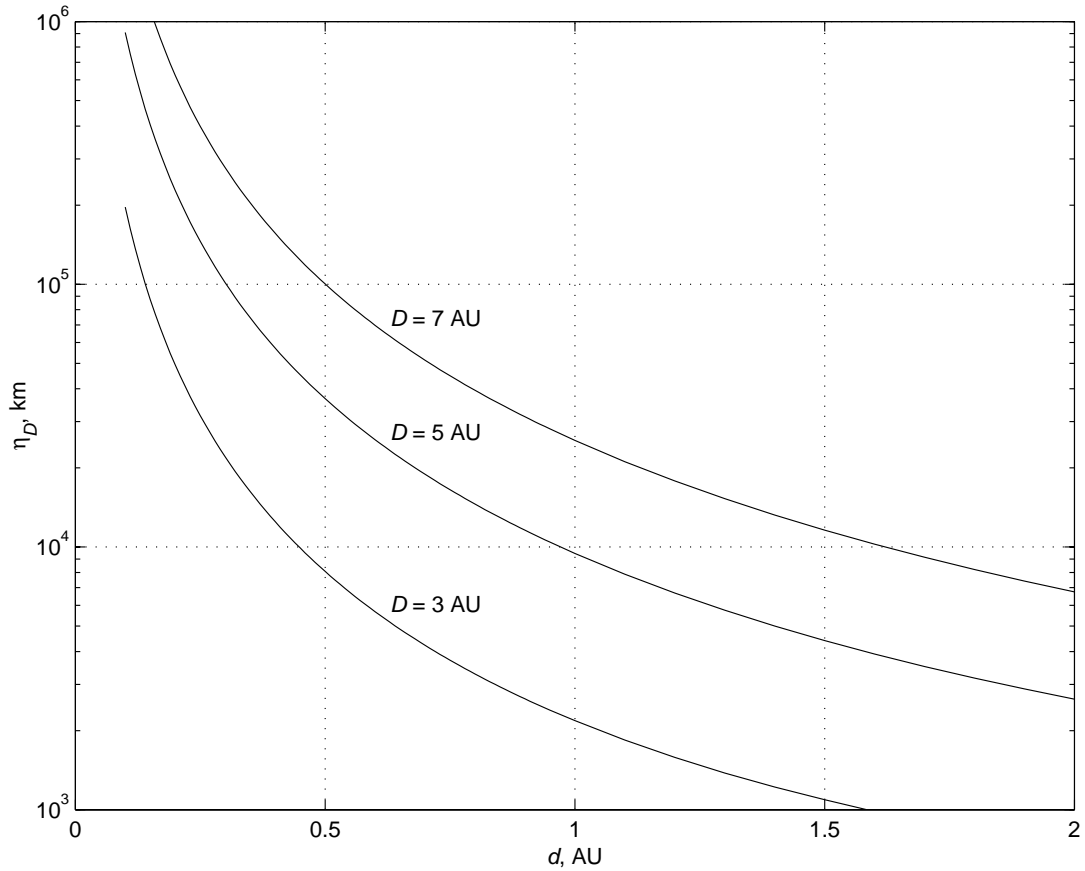


Figure 27. Orbit geometry for range measurements



**Figure 28. Error in heliocentric distance of comet**

will significantly improve the orbit determination. From this figure it is seen that the comet would have to be closer than 3 AU before the angular measurements would provide the 1000 km accuracy assumed for the range measurements.

The results presented in this section reveal an important relationship between parallax and orbit determination accuracy. In all previous analysis, the distance between the comet and the observatory is large enough so that the comet appears to be stationary during the tracking duration. When the tracking time scales are small compared to the time it takes the comet to reach the Earth, the time rate of change of parallax is an important parameter and observatory orbits with smaller radii perform well. On the other hand, over longer time scales the total parallax is the important parameter. In this case observatory orbits with larger

radii are better. So a trade should be made concerning the amount of time between the discovery of the comet and the time when a collision is predicted to occur. If observing time on the order of years is available, an observatory outside a heliocentric radius of 1 AU will perform well because both the observatory motion and the comet motion help in the orbit determination accuracy. If not much time is available for collecting observations an observatory inside 1 AU will perform well because of the higher time rate of change of parallax.

## 6 Summary and Conclusions

This research investigated the effect of tracking duration and observatory placement on orbit determination accuracy for a set of Earth-impacting, long-period comets with various orbit inclinations. Orbit solutions were obtained using a Kalman filter algorithm, in which an assumption is made that the comet orbit dynamics can be described by a linear model. Orbit determination accuracy results have been presented in terms of Earth collision probability. Perturbations due to comet outgassing were included in this analysis, and have been shown to be negligible until the comet reaches a heliocentric distance of 2.5 AU, which is approximately 200 days of tracking from an initial distance of 5 AU. Perturbations in comet position are less than 1 Earth radius at a heliocentric distance of 1 AU. Monte Carlo simulations proved that the Kalman filter linearity assumption is valid, even when comet outgassing is present.

It was determined that the best observatory location is one in which the rate of parallax change is maximum based upon a brief study concerning the relationship between the time rate of change of parallax between the observatory and the comet and orbit determination accuracy. This occurs when the motion of the observatory is perpendicular to the Sun-comet line. Circular heliocentric observatory orbits with radii of 0.5 AU and 3 AU both have maximum parallax rates that are larger than that of an observatory orbit at 1 AU. The smallest maximum parallax rate within the inner solar system occurs in an orbit with a radius of approximately 1.7 AU. A comparison of collision probability results obtained from observatories in Mercury, Venus, Earth, and Mars orbits confirmed these findings, and in general the Mercury and Venus observatories performed better than the Earth observatory, while the Mars observatory performed worse in all instances. However, because longer tracking intervals increased the orbit determination accuracy of the Earth observatory to

match or exceed the accuracy of the observatory orbits with smaller radii, it was concluded that the additional cost of transfer and maintenance for an observatory outside 1 AU was not justifiable.

A solution is considered accurate when collision probability is 0.99 or above for Earth observatory orbit determination. For a single Earth observatory with 0.1 arcsecond resolution, four months of daily observations is required to accurately determine the orbit of an outgassing comet. Adding an observatory positioned at the Sun-Earth Lagrange point  $L_4$  reduces the necessary tracking duration to three months, and including yet another observatory at the Sun-Earth  $L_5$  Lagrange point reduces the tracking duration to approximately two and a half months. The best orbit determination results from a single Earth observatory with range measurement capability good to 1000 km, which can achieve 0.99 collision probability with only 51 days of tracking. Similar accuracy is obtained by a system of two observatories with an angular separation of  $180^\circ$ .

All of the observatory configurations studied are capable of producing collision probabilities of 0.99 or better. The reason why one configuration is deemed “better” than another is because the required orbit determination accuracy is obtained in less time. In fact, all configurations are capable of producing collision probabilities as high as 0.999999 within the assumptions of the study if the tracking duration is long enough. No matter how many observatories are used or where in the inner solar system they are located, increasing the tracking interval will always improve orbit determination accuracy.

## 7 Future Work

Confirming such high collision probability as 0.999999 will require a much more detailed analysis than presented here, where additional force and observation error models should be included. The force models should include solar radiation pressure where uncertainty in comet mass is a consideration. The error models should include ephemeris errors, especially if the comet makes a close approach to Jupiter or Mars on the inbound leg of the impacting trajectory, and correlation between observations due to atmospheric effects should be included. Instrument biases should also be included, because actual error distributions will be much more complex than the simple normal distribution assumed in this analysis. Finally, a more consistent outgassing error model should be implemented. A time-varying element of uncertainty due to comet outgassing was included in the covariance  $\mathbf{Q}(t)$  which was updated once per day during the tracking intervals when observations were being collected, and approximately once every two weeks during the propagation from the time of the last observation to the designed time of collision. An appropriate time interval between updates to the covariance  $\mathbf{Q}(t)$  should be determined and applied consistently throughout the analysis.

## References

1. Friedman, G., “Risk Management of Planetary Defense”, AIAA Paper 96-4389, AIAA Meeting Papers on Disc, September 1996.
2. Chodas, P. W., et al., “Automated Detection of Potentially Hazardous Near-Earth Encounters”, AAS 01-461, AAS/AIAA Astrodynamics Specialists Conference, Quebec City, Quebec, Canada, July 30 – August 2, 2001.
3. Noll, K. S., Weaver, H. A., and Feldman, P. D., *The Collision of Comet Shoemaker-Levy 9 and Jupiter: IAU Colloquium 156, proceedings of the Space Telescope Science Institute Workshop in Baltimore, Maryland, May 9 – 12, 1995*, Cambridge University Press, New York, 1996.
4. Battin, R. H., *An Introduction to the Mathematics and Methods of Astrodynamics, Revised Edition*, AIAA, Reston, VA, 1999.
5. Bate, R. R., Mueller, D. D., and White, J. E., *Fundamentals of Astrodynamics*, Dover Publications, Inc., New York, 1971.
6. Sagan, C., and Druyan, A., *Comet*, Ballantine Books, New York, 1997.
7. Marsden, B. G., Sekanina, Z., and Yeomans, D. K., “Comets and Nongravitational Forces, V”, *The Astronomical Journal*, Vol.78, No.2, 1973.
8. Ekelund, J. E., and Yeomans, D. K., “A Program for the Accurate Generation of Ephemerides for Halley’s Comet”, AAS 85-350.
9. Roithmayr, Carlos, NASA Langley Research Center, *private communication*, 2001-2003.
10. Gelb, A., *Applied Optimal Estimation*, The M.I.T. Press, Cambridge, MA, 1986.
11. Maybeck, P. S., *Stochastic Models, Estimation, and Control, Volume 1*, Navtech Book & Software Store, Arlington, VA, 1994.
12. Chodas, P. W., and Yeomans, D. K., “Orbit Determination and Estimation of Impact Probability for Near Earth Objects”, AAS 99-002, *Advances in the Astronautical Sciences* 101 (1999): 21-40.

# Appendix

The set of six classic Keplerian orbital elements defined in Ref. [5] are

1.  $a$ , semimajor axis;
2.  $e$ , eccentricity;
3.  $i$ , inclination;
4.  $\Omega$ , longitude of ascending node;
5.  $\omega$ , argument of periapsis;
6.  $\tau$ , time of periapsis passage.

The first two orbital elements determine the size and shape of the orbit. The next three elements are Euler angles that determine the orbit orientation in three-dimensional space.

The sixth orbital element is used to determine the position of the object at a particular time.

If the position,  $\mathbf{r}$ , and velocity,  $\mathbf{v}$ , of the object are known, calculating the orbital elements is a straightforward process. To accomplish this, determine three important vectors: the angular momentum vector  $\mathbf{h}$ , the node vector  $\mathbf{n}$ , and the eccentricity vector  $\mathbf{e}$ . These vectors are shown in Fig. A1, which shows the orientation of the orbit plane in 3-dimensional

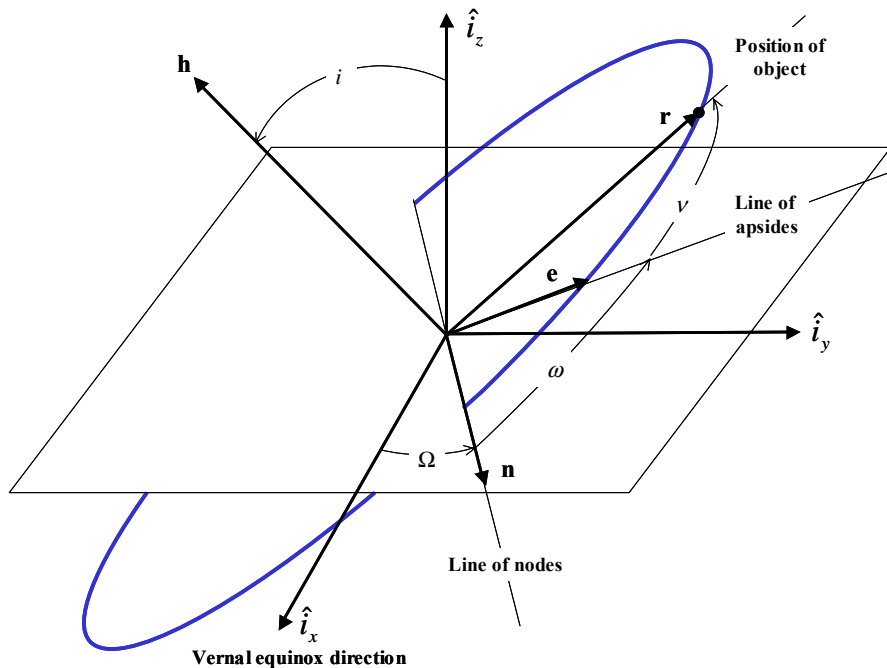


Figure A1. Orbital plane orientation in 3-dimensional space

space. The angular momentum vector is normal to the orbit plane and is given by

$$\mathbf{h} = \mathbf{r} \times \mathbf{v}. \quad (\text{A1})$$

The node vector is defined as

$$\mathbf{n} \equiv \hat{i}_z \times \mathbf{h}, \quad (\text{A2})$$

and lies in both the orbit and ecliptic plane. The intersection of these planes is referred to as the line of nodes, and  $\mathbf{n}$  points in the direction of the ascending node. If  $\mathbf{h}$  is parallel to  $\hat{i}_z$ , then  $\mathbf{n} = \hat{i}_x$ . The eccentricity vector is expressed as Eq. (3.14) of Ref. [4],

$$\mathbf{e} = \frac{1}{\mu} (\mathbf{v} \times \mathbf{h}) - \frac{\mathbf{r}}{r}, \quad (\text{A3})$$

where  $r$  is the magnitude of the position of the object. For elliptic orbits, the vector  $\mathbf{e}$  originates at the focus of the orbit and lies along a line called the line of apsides. There are two important points in the orbit which lie on the line of apsides: periapsis and apoapsis. The eccentricity vector points toward periapsis, the point on the orbit where the object is closest to the primary body. The distance to this point is denoted  $r_p$ . Apoapsis is the point where the object is farthest from the primary body, and the distance to this point is denoted  $r_a$ . Expressions for periapsis and apoapsis are given by

$$r_p = \frac{p}{1+e}, \quad (\text{A4})$$

and

$$r_a = \frac{p}{1-e}, \quad (\text{A5})$$

where  $p$  is the semi-latus rectum,

$$p = \frac{h^2}{\mu}. \quad (\text{A6})$$

When the Sun is the primary body,  $r_p$  and  $r_a$  are referred to as perihelion and aphelion, respectively.

With the three vectors  $\mathbf{h}$ ,  $\mathbf{n}$ , and  $\mathbf{e}$  determined, the orbital elements are simple to obtain as follows:

1. Calculate the magnitude of the eccentricity vector, i.e.,

$$e = (\mathbf{e} \cdot \mathbf{e})^{1/2}. \quad (\text{A7})$$

2. Determine the semimajor axis using the expression

$$a = \frac{r}{2} - \frac{\mu}{v^2}, \quad (\text{A8})$$

where  $v$  is the magnitude of the velocity of the object.

3. The inclination is the angle between  $\hat{i}_z$  and  $\mathbf{h}$ , therefore

$$\cos i = \frac{\mathbf{h} \cdot \hat{i}_z}{h}, \quad (\text{A9})$$

where  $h$  is the magnitude of  $\mathbf{h}$ , and  $0^\circ \leq i \leq 180^\circ$ .

4. The ascending node is the angle between  $\hat{i}_x$  and  $\mathbf{n}$ , hence

$$\sin \Omega = \frac{\mathbf{n} \cdot \hat{i}_y}{n}, \quad \cos \Omega = \frac{\mathbf{n} \cdot \hat{i}_x}{n}, \quad (\text{A10})$$

where  $n$  is the magnitude of  $\mathbf{n}$ .

5. The argument of periapsis is the angle between  $\mathbf{n}$  and  $\mathbf{e}$ , therefore

$$\sin \omega = \frac{\mathbf{e}}{e} \cdot \left( \frac{\mathbf{h} \times \mathbf{n}}{hn} \right), \quad \cos \omega = \frac{\mathbf{n} \cdot \mathbf{e}}{ne}. \quad (\text{A11})$$

6. Determine the time of periapsis passage from Kepler's equation,

$$M = n(t - \tau) = E - e \sin E, \quad (\text{A12})$$

where  $n$  is the mean motion given by

$$n = \sqrt{\frac{\mu}{a^3}}, \quad (\text{A13})$$

and  $M$  is the mean anomaly, which describes an angle that evolves linearly with time. The mean anomaly has no significance other than convenience of notation.

The eccentric anomaly,  $E$ , is expressed in terms of the true anomaly,  $\nu$ , as

$$\cos E = \frac{e + \cos \nu}{1 + e \cos \nu}, \quad \sin E = \frac{\sqrt{1 - e^2} \sin \nu}{1 + e \cos \nu}, \quad (\text{A14})$$

where

$$\cos \nu = \frac{\mathbf{e} \cdot \mathbf{r}}{er}, \quad \sin \nu = \frac{v_r}{e} \sqrt{\frac{p}{\mu}}, \quad (\text{A15})$$

and  $v_r$  is the velocity along the radial direction, i.e.,

$$v_r = \frac{\mathbf{r} \cdot \mathbf{v}}{r}. \quad (\text{A16})$$

Conversely, the position and velocity of the object can be determined from a set of orbital elements and a specified time. First solve Kepler's equation for  $E$  and then solve Eq. (A15) for  $v$ . Calculate the magnitude of the position,  $r$ , using the equation of the orbit,

$$r = \frac{p}{1 + e \cos v}. \quad (\text{A17})$$

Next, determine the position vector using the 3-1-3 Euler angle rotation  $[\Omega, i, \psi]$  starting with  $[r, 0, 0]$ , i.e.,

$$\mathbf{r} = r \begin{bmatrix} (\cos \psi \cos \Omega - \sin \psi \sin \Omega \cos i) \hat{i}_x \\ (\cos \psi \sin \Omega + \sin \psi \cos \Omega \cos i) \hat{i}_y \\ (\sin \psi \sin i) \hat{i}_z \end{bmatrix} \quad (\text{A18})$$

where  $\psi = \omega + v$ . Calculate the magnitude of the velocity from the vis-viva integral,

$$v^2 = \mu \left( \frac{2}{r} - \frac{1}{a} \right). \quad (\text{A20})$$

Finally, determine the velocity vector using the 3-1-3 Euler angle rotation  $[\Omega, i, \psi]$  starting with  $[v_r, r \frac{d\psi}{dt}, 0]$ , i.e.,

$$\mathbf{v} = v_r \begin{bmatrix} (\cos \psi \cos \Omega - \sin \psi \sin \Omega \cos i) \hat{i}_x \\ (\cos \psi \sin \Omega + \sin \psi \cos \Omega \cos i) \hat{i}_y \\ (\sin \psi \sin i) \hat{i}_z \end{bmatrix} + r \frac{d\psi}{dt} \begin{bmatrix} (-\sin \psi \cos \Omega - \cos \psi \sin \Omega \cos i) \hat{i}_x \\ (-\sin \psi \sin \Omega + \cos \psi \cos \Omega \cos i) \hat{i}_y \\ (\cos \psi \sin i) \hat{i}_z \end{bmatrix} \quad (\text{A21})$$

where  $v_r$  is the component of velocity along the radial direction,  $r \frac{d\psi}{dt} = \frac{h}{r}$ , and  $h = \sqrt{\mu p}$ .